

Robust Omnidirectional Aerial Manipulation for Enlarged Workspace

Journal Title
XX(X):1–17
©The Author(s) 2016
Reprints and permission:
sagepub.co.uk/journalsPermissions.nav
DOI: 10.1177/ToBeAssigned
www.sagepub.com/



Dongjae Lee*, Byeongjun Kim*, and H. Jin Kim

Abstract

This work presents a geometric robust control and whole-body motion planning framework for an omnidirectional aerial manipulator (OAM). Compared to existing ground mobile manipulators and aerial manipulators, our robot is capable of freely locating at arbitrary position and orientation, expanding the workspace for manipulation. To fully exploit the merit of an OAM, we first propose a geometric robust controller for a floating base. Since the motion of the robotic arm and interaction wrench during manipulation affects the floating base, the base should be capable of attenuating these adverse effects in controlling its 6D pose. Next, we design a two-step whole-body motion planner. The pose of the floating base and the joint angles of the robotic arm are jointly considered in motion planning to harness the entire configuration space. The proposed methods allow the manipulator base to be fixed at any 6D pose while autonomously accomplishing sophisticated manipulation. We demonstrate effectiveness of the proposed framework through experiments where an OAM performs grasping-and-pulling an object in multiple scenarios including near 90° and even 180° pitching.

Keywords

mobile manipulation, aerial manipulation, geometric control, robust control, whole-body motion planning, model predictive control

1 Introduction

1.1 Background and motivation

Mobile manipulators with various base platforms (quadruped [Sleiman et al. \(2021\)](#), ball-balancing robot [Minniti et al. \(2019\)](#), multirotor [Wang et al. \(2023\)](#)) have been introduced to expand the workspace of the manipulator. In particular, thanks to the capability to locate itself in wider workspace, aerial manipulators utilizing aerial robots as a base have been actively studied [Ollero et al. \(2022\)](#). However, existing aerial manipulators based on conventional multirotors can conduct manipulation only in small roll, pitch angles due to the underactuatedness of the multirotor base. If additional freedom exists for a multirotor base to hover at arbitrary orientation, the workspace of the manipulator can be considerably enlarged, and such enlarged workspace may enable a manipulation task that is originally not viable. Although aerial manipulators based on a fully actuated multirotor base [Ryll et al. \(2019\)](#) are studied in [Tognon et al. \(2019\)](#); [Nava et al. \(2020\)](#) to provide hoverability in non-zero roll, pitch angles, there still exist non-trivial regions in orientation space (e.g. near 90° pitch angle) where the multirotor cannot hover. Several studies have been proposed to enhance versatility by serially connecting multiple aerial robots [Zhao et al. \(2018, 2023\)](#). However, when the task involves object grasping, these platforms require substantially large, collision-free workspace as they utilize aerial robot modules to enclose the object.

In this study, we aim to investigate a mobile manipulator that can locate the floating base in any 3D space with arbitrary position and orientation, as depicted in Fig. 1. To achieve this goal, we consider an omnidirectional

aerial manipulator (OAM) which is a combination of an omnidirectional multirotor [Allenspach et al. \(2020\)](#) and a multi-degrees-of-freedom (multi-DoF) robotic arm. Our study focuses on addressing two main issues: developing a method 1) to stably control the position and orientation of the multirotor base regardless of the arm movement or manipulation task, and 2) to enable whole-body motion planning while utilizing the omnidirectionality of the multirotor's orientation and taking into account the surrounding environment for collision avoidance and manipulation.

1.2 Problem description

First, from a control perspective, two types of techniques are required: geometric control technique allowing the control input to be defined at arbitrary orientation on SO(3) and robust control technique capable of providing robustness irrespective of the arm movement or manipulation. If a local representation like Euler angles is used to express the orientation of the multirotor, it may become unstable near the 90° pitch angle due to the singularity issue, preventing

*The first two authors contributed equally to this work.

The authors are with the Department of Aerospace Engineering and the Automation and Systems Research Institute (ASRI), Seoul National University, Seoul 08826, South Korea

Corresponding author:

H. Jin Kim, Department of Aerospace Engineering and the Automation and Systems Research Institute (ASRI), Seoul National University, Seoul 08826, South Korea.

Email: hjinkim@snu.ac.kr

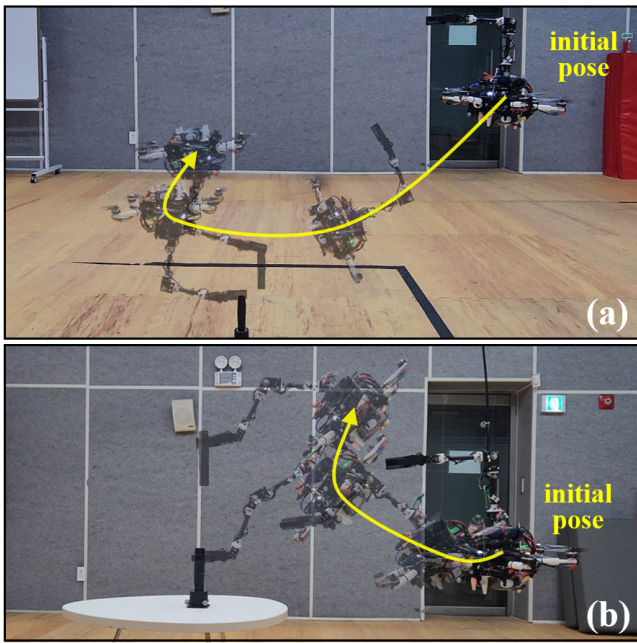


Figure 1. An omnidirectional aerial manipulator (OAM) conducting a precise manipulation task of grasping-and-pulling a bar (a) on the ground and (b) on a table. The whole-body motion is computed from the proposed cascaded motion planner, and the reference trajectory is tracked by the proposed geometric robust controller.

the full utilization of omnidirectionality. Additionally, if the position and orientation of the base are not properly regulated by the movement of the robotic arm or the manipulation task, it may lead to failure in sophisticated manipulation tasks. Such tracking error can result in collision with the surrounding environment, leading to a crash. Although the two issues have been tackled individually for aerial manipulators, to the best of the authors' knowledge, they have not been resolved simultaneously for OAM.

Next, from a planning perspective, it is essential to perform whole-body motion planning that considers both the position and orientation of the multirotor base, as well as the joint angles of the robotic arm. In doing so, it is necessary to: 1) consider the non-Euclidean configuration space $\text{SO}(3)$ of orientation, and 2) enable online replanning. If motion planning is conducted separately for the multirotor and robotic arm, the search space of the planning problem is restricted, potentially resulting in sub-optimality or infeasibility despite the existence of feasible solutions. Additionally, when using local parameterization such as Euler angles to represent the orientation of the multirotor base, solution may not be obtained in certain initial conditions due to degeneracy of such local parameterization. Finally, to respond promptly to uncertainties especially during manipulation, online replanning capability is required.

1.3 Method overview and contribution

To resolve these problems, we first propose a geometric robust integral of the tanh of the error (gRITE) controller. The proposed controller augments an integral of the tanh of the error term to a geometric nonlinear PID controller Goodarzi et al. (2013) which has been applied to most

existing OAMs Su et al. (2023); Zhao et al. (2023); Bodie et al. (2021b), and stability of the closed-loop system is formally analyzed. The added integral term is shown to be effective in suppressing the ultimate error bound, which can be made arbitrarily small with sufficiently large control gain. Next, we propose a two-step trajectory-optimization-based whole-body motion planning method. There exist two main computation bottlenecks in applying optimization-based algorithms which may hinder real-time computation and even convergence of the solution: 1) high-dimensional, non-convex search space and 2) non-Euclidean space of $\text{SO}(3)$.* To overcome these bottlenecks, we divide the problem into two steps where the first step solves an end-effector level subproblem, and the whole body motion considering end-effector trajectory tracking, whole-body kinematics, and physical constraints is computed in the second step.

We conduct comparative experiments for the proposed controller where the proposed one outperforms the counterpart (i.e. geometric nonlinear PID controller) in regulating both position and orientation in the presence of the robotic arm's motion. Then, the proposed control and planning framework is experimentally validated where an omnidirectional aerial manipulator (OAM) (Fig. 2) performs grasping-and-pulling tasks in various environments requiring precise manipulation. Mobile manipulation using the OAM is successfully executed in five different scenarios: 1) ground-basic, 2) ground-yaw, 3) ground-pitch, 4) table-far, and 5) table-close which are illustrated in Figs. 7, 9. Through the experiments, we demonstrate precise control performance regardless of disturbance, such as the movement of the robotic arm and ground effect, at arbitrary position and orientation of the base. Furthermore, the proposed planning algorithm is shown to effectively utilize whole-body motion including omnidirectionality of the floating base in conducting the manipulation task while taking into account multiple physical constraints in real-time faster than 10 Hz.

In summary, the main contribution of this work can be summarized as follows:

- We present a gRITE (geometric Robust Integral of the Tanh of the Error) controller for an omnidirectional multirotor base to enable precise mobile manipulation of the OAM. We formally prove that the proposed controller guarantees arbitrarily small ultimate bound with sufficiently large control gains.
- We present a two-step trajectory-optimization-based whole-body motion planning method for an omnidirectional aerial manipulator with a multi-DoF robotic arm. The proposed method is capable of online replanning in a confined space faster than 10 Hz and exploiting the entire space of $\text{SO}(3)$.
- We conduct multiple experiments where an OAM with a multi-DoF robotic arm performs grasping-and-pulling an object either on the ground or

*Simultaneously considering not only the position and orientation of the floating base but also the joint angles of the robotic arm increases the dimension of the search space, and the non-convexity comes from collision avoidance constraints. Moreover, to represent the orientation of the base in a non-Euclidean space, nonlinear parameterizations such as quaternions or rotation matrices must be employed.

Table 1. Comparison with state-of-the-art works on omnidirectional aerial manipulators

Study	OAM platform		Control		method	Motion planning		
	multirotor (# of actuators)	manipulator (DoF)	method	disturbance rejection		whole-body kinematics	collision avoidance	online replanning
Ours	tiltable (12)	serial (4)	gRITE	✓	two-step TO[†]	✓	✓	✓
Bodie et al. (2021b)	tiltable (12)	parallel (3)	FF + PID	△*	IK [‡]	✗ [‡]	✗	✓
Su et al. (2023)	tiltable (16)	serial (3)	PID	△	VKC [†]	△ [§]	✓	✗
Brunner et al. (2022)	tiltable (12)	fixed (0)	impedance	✗	MPPI [†]	△ [¶]	✗	✓
Zhao et al. (2023)	tiltable (16)	fixed (0)	PID	△		N/A (wrench planning)		
Bodie et al. (2021a)	tiltable (12)	fixed (0)	force & impedance	✗		N/A (force planning)		

*: FF(Feed Forward) term requires the acceleration measurement, and the performance against other disturbances rely solely on PID.

†: Trajectory Optimization (TO), Inverse Kinematics (IK), Virtual Kinematic Chain (VKC), Model Predictive Path Integral Control (MPPI).

‡: Whole-body motion is not jointly tackled in that only the joint angles are considered.

§: Singularity issue may occur due to the use of Euler angles.

¶: No joint angle is considered, but there is a possibility of extension to OAM with a multi-DoF manipulator.

on a table, which would not be possible for a conventional underactuated aerial manipulator with the same manipulator configuration. They demonstrate effectiveness and applicability of the proposed controller and planner.

1.4 Notations

For column vectors \mathbf{a} and \mathbf{b} , $[\mathbf{a}; \mathbf{b}] := [\mathbf{a}^\top \ \mathbf{b}^\top]^\top$. For a vector $\mathbf{v} \in \mathbb{R}^n$ and a diagonal matrix $\mathbf{W} \in \mathbb{R}^{n \times n}$, v_i and W_i indicate the i^{th} element, respectively. $\|\mathbf{v}\|$ denotes Euclidean norm of a vector $\mathbf{v} \in \mathbb{R}^n$, and we also introduce $\|\mathbf{v}\|_{\mathbf{P}}^2 := \mathbf{v}^\top \mathbf{P} \mathbf{v}$ for a weight matrix $\mathbf{P} \in \mathbb{R}_{>0}^{n \times n}$. \mathbf{I}_n is the identity matrix in $\mathbb{R}^{n \times n}$. $(\cdot)^\wedge$ is a hat map that maps a vector in \mathbb{R}^3 to a skew-symmetric matrix such that $\mathbf{v} \times \mathbf{w} = \mathbf{v}^\wedge \mathbf{w}$ for any $\mathbf{v}, \mathbf{w} \in \mathbb{R}^3$. The vee map $(\cdot)^\vee$ is an inverse map of the hat map. $c*, s*$ denote shorthands for $\cos(*)$ and $\sin(*)$, respectively. The Minkowski sum between two sets \mathcal{A}, \mathcal{B} are defined as $\mathcal{A} \bigoplus \mathcal{B}$. Lastly, for a given set \mathcal{S} , \mathcal{S}^c stands for the complement of \mathcal{S} .

2 Related work

In this section, we discuss related work on control and whole-body motion planning for the developed OAM. Comparison with existing state-of-the-art works on OAMs is summarized in Table 1.

2.1 Control

The first objective of this study is to design a geometric robust controller for an omnidirectional aerial manipulator (OAM). Accordingly, we first review robust or geometric robust control techniques applied to conventional aerial manipulators, then investigate control methods applied to an OAM. Lastly, we discuss related work on the proposed control technique, which is the geometric robust integral of the tanh of the error (gRITE).

Dynamic coupling effect exists between a multirotor base and a rigidly attached robotic arm Kim et al. (2017), and the base can become unstable if this coupling effect is not suitably addressed in a controller Huber et al. (2013). To resolve this problem, various studies on a conventional multirotor-based aerial manipulator Lee et al. (2022); Kim et al. (2017); Lee et al. (2021); Liang et al. (2023) design robust controllers where the motion of the robotic arm is treated as external disturbance. However, their use of Euler

angles in attitude control renders the controllers numerically unstable near 90° pitch angle, limiting their applicability to an OAM. Although Yu et al. (2020) proposes a geometric robust controller using orientation error directly defined on SO(3), its validation is limited to simulation, and its performance may degrade when applied to a real robot due to the control law not being Lipschitz continuous.

Studies on an OAM utilize a controller considering the non-Euclidean property of SO(3) to fully harness the omnidirectionality of the robot. However, as they consider only an OAM with a zero-DoF robotic arm Bodie et al. (2021a); Brunner et al. (2022); Cuniato et al. (2023), robustness against the relative motion of the robotic arm to the multirotor base is not tackled in their controllers. An OAM with a multi-DoF parallel robotic arm is considered in Bodie et al. (2021b), and the authors design a controller with a feedforward term to compensate for the dynamic coupling effect of the robotic arm. However, as the method requires a precise dynamical model of the coupling effect and acceleration measurement, the performance may degrade when external disturbance (e.g. interaction wrench while grasping an object of an unknown mass) or excessive measurement noise exists. Su et al. (2023) presents a nonlinear PID controller for an OAM equipped with a multi-DoF serial robotic arm, but its performance in disturbance attenuation may be insufficient for precise manipulation tasks like grasping-and-pulling.

This study proposes a gRITE controller, which is an extension to a RISE (robust integral of the sign of the error) controller first presented in Xian et al. (2004). The RISE control achieves asymptotic stabilizability for an uncertain system using a continuous control input, and it has been adopted in various platforms Kamaldin et al. (2019); Deng and Yao (2021); Shin et al. (2011). However, due to the derivative of the control input not being continuous, input chattering may occur when applying high gains. Accordingly, in the hardware perspective where desired force/torque is tracked by actuators, the actuators' tracking performance may deteriorate, resulting in overall performance degradation. To alleviate such problem, Kidambi et al. (2021) replaces the sign function with the tanh function when validating its controller in simulation, but analysis for the replaced tanh function is not conducted. The original stability analysis with the sign function can no longer be applied to our case where the sign function

is substituted by the tanh function because there appears a residual term in the derivative of the Lyapunov function that cannot be shown to be non-positive. [Xian and Zhang \(2016\)](#) presents formal stability analysis for a smooth counterpart of the RISE control using the tanh function, but the analysis is conducted only in \mathbb{R}^n space. A geometric RISE controller is designed in [Gu et al. \(2022\)](#) and is applied to a quadrotor, but its analysis is built upon a lemma that is not applicable to a case with external disturbance (Lemma 1 showing boundedness of the attitude error function), and the input chattering issue that may occur by high gains is not taken into account.

2.2 Whole-body motion planning

Our second objective is to present a whole-body motion planner exploiting the omnidirectionality of an OAM while abiding by various state constraints such as collision avoidance. Considering this objective, we first review whole-body planning techniques for ground robot-based mobile manipulators. Then, we investigate planning algorithms designed for aerial manipulators including OAMs. Lastly, we discuss related work on optimization-based motion planning where the whole configuration space of orientation, i.e. SO(3), is addressed.

A whole-body motion generation algorithm developed for a mobile manipulator whose base is a planar wheeled robot can be found in [Zhang et al. \(2020\)](#). Planar mobile robots only demand single scalar values representing heading angles to fully describe the orientation whereas at least 3 variables are needed for the OAM's base. Thus, it is not directly applicable to the OAM. Quadruped robots have widely been used as bases of mobile manipulators [Sleiman et al. \(2021\)](#); [Arcari et al. \(2023\)](#); [Chiu et al. \(2022\)](#). However, since they conduct mobile manipulation while maintaining the pedals to have a stable contact with the ground, roll and pitch angles of the base orientation is restricted below 90°. Accordingly, they rely on Euler angles to represent the base orientation. Meanwhile, the OAM is capable of hovering with arbitrary base pose. Thus, to fully utilize such capability during manipulation while applying the methods for quadruped robots, one should additionally consider the entire SO(3) and the corresponding nonlinear kinematics.

Similarly, existing studies on aerial manipulators [Lee et al. \(2020\)](#); [Lee and Kim \(2017\)](#) have limitations in that they utilize Euler angles in designing a motion planner. Although there exist studies employing the whole configuration space of SO(3) [Tognon et al. \(2018\)](#); [Welde et al. \(2021\)](#), their approaches do not tackle state constraints including obstacle and self-collision avoidance and are only validated in simulation. As presented in the previous subsection, many studies on OAM consider a platform equipped with a zero-DoF manipulator [Bodie et al. \(2021a\)](#); [Brunner et al. \(2022\)](#); [Cuniato et al. \(2023\)](#). Among these, only [Brunner et al. \(2022\)](#) tackles a problem of motion planning for OAM, but manipulator-related constraints including self-collision avoidance are not considered. Recent work [Su et al. \(2023\)](#) also investigates whole-body motion planning for an OAM with a multi-DoF manipulator. However, the authors represented OAM's base orientation using only three angles,

leading to singularity issues, and the method can only be computed offline.

There have been several studies to entirely consider the configuration space SO(3) in optimization-based motion planning. In [Sun et al. \(2022\)](#), a nonlinear MPC formulated using unit quaternion is applied to an agile flight of a quadrotor. [Brescianini and D'Andrea \(2018\)](#) designs motion primitives by using a rotation vector and a closed-form solution of an acceleration-minimizing optimization problem for a fully actuated multirotor. [Ding et al. \(2021\)](#) and [Wehbeh and Sharf \(2022\)](#) formulate an MPC problem for quadruped and quadrotor with bidirectional thrust, respectively, where a rotation matrix is utilized by applying a variation-based linearization technique. [Meduri et al. \(2023\)](#) suggests an efficient MPC solver for walking robots by exploiting a structure of centroidal dynamics. In [Kalabić et al. \(2017\)](#), MPC is designed for a system with dynamics defined on a smooth manifold, and stability is theoretically analyzed. However, all the mentioned studies do not take into account state constraints for avoiding self-collision of a manipulator or obstacle collision since application to mobile manipulators is not considered in these works.

3 Controller design

The objectives in our controller design are the following two:

- robustness to external disturbance and model uncertainty to ensure robustness against multiple sources of disturbance including the robotic arm's motion and ground effect and model uncertainty arising from an object at the end-effector.
- well-defined control law in all state space without singularity to fully exploit the omnidirectionality of the aerial robot which can be hindered if using local coordinates such as Euler angles for representing orientation.

To achieve these objectives, we propose a *geometric Robust Integral Tanh of the Error* (gRITE) controller which guarantees ultimate boundedness of the closed-loop system with arbitrarily small ultimate bound by choosing proper control gains.

3.1 System dynamics

We consider the following system dynamics:

$$m\ddot{\mathbf{p}} = \mathbf{R}\mathbf{f} - mg\mathbf{b}_3 + \mathbf{d}_t \quad (1a)$$

$$J_b\dot{\omega} = -\omega^\wedge J_b\omega + \tau + \mathbf{d}_r \quad (1b)$$

where $\mathbf{p} \in \mathbb{R}^3$, $\mathbf{R} \in \text{SO}(3)$, $\omega \in \mathbb{R}^3$ are the position, orientation and body angular velocity of the multirotor base, respectively. (1a) models translational dynamics and (1b) is for rotational dynamics. $\mathbf{d}_t, \mathbf{d}_r \in \mathbb{R}^3$ are external disturbance in translational and rotational dynamics. We denote the gravitational acceleration as $g \in \mathbb{R}_{>0}$, and $m \in \mathbb{R}_{>0}$, $J_b \in \mathbb{R}_{>0}^{3 \times 3}$ are mass and moment of inertia of the aerial manipulator measured at a certain configuration of the robotic arm while $\mathbf{b}_3 = [0; 0; 1]$. The motion of the robotic arm induces a change in the moment of inertia of the aerial manipulator J_b and reaction force and torque to the multirotor, and these are considered as model uncertainty

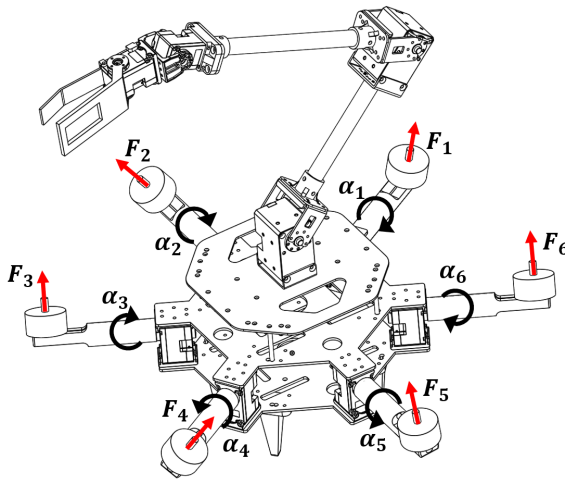


Figure 2. CAD for the omnidirectional aerial manipulator. Actuator inputs are visualized which are rotor thrust $\mathbf{F} = [F_1, \dots, F_6]$ and servo angle $\alpha = [\alpha_1, \dots, \alpha_6]$.

in J_b and external disturbance d_t and d_r , respectively. If the end-effector of the robotic arm grasps an object, then the added inertia of the attached object is accounted as uncertainty in m and J_b since the added inertia is generally unknown. Control inputs are force $\mathbf{f} \in \mathbb{R}^3$ and torque $\boldsymbol{\tau} \in \mathbb{R}^3$ represented in the multirotor body frame, indicating fully actuatedness.

3.2 Control allocation

The OAM considered in this paper is illustrated in Fig. 2. The omnidirectional multirotor base consists of six rotors and six servomotors. As visualized in Fig. 2, actuator inputs are $F_i \in \mathbb{R}_{>0}$ and $\alpha_i \in \mathbb{R}$, which are thrust of the i^{th} rotor and servo angle of the i^{th} servomotor, respectively. To realize a control input $[\mathbf{f}; \boldsymbol{\tau}] \in \mathbb{R}^6$ in the multirotor, control allocation is required which solves a problem of finding actuator inputs $\mathbf{F} = [F_1, \dots, F_6]^\top \in \mathbb{R}^6$ and $\boldsymbol{\alpha} = [\alpha_1, \dots, \alpha_6]^\top \in \mathbb{R}^6$ for given control input $[\mathbf{f}; \boldsymbol{\tau}]$. Using the variable transformation method in Kamel et al. (2018), the relationship between the actuator inputs $\mathbf{F}, \boldsymbol{\alpha}$ and control input $[\mathbf{f}; \boldsymbol{\tau}]$ can be written as

$$\begin{bmatrix} \mathbf{f} \\ \boldsymbol{\tau} \end{bmatrix} = \mathbf{A}\mathbf{b}, \quad \mathbf{b} = \begin{bmatrix} F_1 c\alpha_1 \\ F_1 s\alpha_1 \\ \vdots \\ F_6 c\alpha_6 \\ F_6 s\alpha_6 \end{bmatrix} \quad (2)$$

where $\mathbf{A} \in \mathbb{R}^{6 \times 12}$ is a constant matrix, whose definition can be found in Appendix 8.1. Such equation is derived from the geometric arrangement of actuators in the multirotor base. We compute the vector \mathbf{b} using a weighted pseudo-inverse of \mathbf{A} as

$$\mathbf{b} = \mathbf{A}_W^\dagger \begin{bmatrix} \mathbf{f} \\ \boldsymbol{\tau} \end{bmatrix} \quad (3)$$

where $\mathbf{A}_W^\dagger = \mathbf{W}\mathbf{A}^\top(\mathbf{W}\mathbf{A}^\top)^{-1}$ for a positive definite weight matrix $\mathbf{W} \in \mathbb{R}_{>0}^{12 \times 12}$. Then, the actuator inputs $F_i, \alpha_i \forall i = 1, \dots, 6$ are calculated as

$$\begin{aligned} F_i &= \sqrt{b_{2i-1}^2 + b_{2i}^2} \\ \alpha_i &= \text{atan2}(b_{2i}, b_{2i-1}) \end{aligned} \quad (4)$$

3.3 The proposed control law: gRITE controller

In this subsection, we construct control laws for \mathbf{f} in the translational dynamics (1a) and $\boldsymbol{\tau}$ in the rotational dynamics (1b).

3.3.1 Translational dynamics We design a controller for the translational part first. We define error variables as

$$\begin{aligned} \mathbf{e}_p &= \mathbf{p}_d - \mathbf{p}, & \mathbf{e}_{t1} &= \dot{\mathbf{e}}_p + \Lambda_t \mathbf{e}_p \\ \mathbf{e}_{t2} &= \dot{\mathbf{e}}_{t1} + \mathbf{e}_{t1}, & \mathbf{e}_t &= [\mathbf{e}_p; \mathbf{e}_{t1}; \mathbf{e}_{t2}] \end{aligned} \quad (5)$$

where $\mathbf{p}_d \in \mathbb{R}^3$, $\Lambda_t \in \mathbb{R}_{>0}^{3 \times 3}$ are the desired position and diagonal control gain. Then, the proposed gRITE controller for the translational dynamics is formulated as follows:

$$\mathbf{f} = \mathbf{f}_n + \mathbf{f}_r \quad (6a)$$

$$\mathbf{f}_n = \bar{m}\mathbf{R}^\top(g\mathbf{b}_3 + \mathbf{K}_{tp}\mathbf{e}_p + \mathbf{K}_{td}\dot{\mathbf{e}}_p + \ddot{\mathbf{p}}_d) \quad (6b)$$

$$\begin{aligned} \mathbf{f}_r &= \mathbf{R}^\top \left\{ (\mathbf{K}_{ti} + \rho_t \mathbf{I}_3)(\mathbf{e}_{t1}(t) - \mathbf{e}_{t1}(0)) + \right. \\ &\quad \left. \int_0^t (\mathbf{K}_{ti} + \rho_t \mathbf{I}_3)\mathbf{e}_{t1}(\tau) + \boldsymbol{\Gamma}_t \text{Tanh}(\boldsymbol{\Theta}_t \mathbf{e}_{t1}(\tau)) d\tau \right\} \end{aligned} \quad (6c)$$

where $(\cdot)_n$, $(\cdot)_r$ indicate the nominal and robust control laws if (\cdot) is a control input, and $\bar{(\cdot)}$ denotes a nominal value of (\cdot) . $\mathbf{K}_{tp}, \mathbf{K}_{td}, \mathbf{K}_{ti}, \boldsymbol{\Gamma}_t, \boldsymbol{\Theta}_t \in \mathbb{R}_{>0}^{3 \times 3}$ and $\rho_t \in \mathbb{R}_{>0}$ are diagonal control gains, and for $\mathbf{v} \in \mathbb{R}^n$, $\text{Tanh}(\mathbf{v}) = [\tanh(v_1); \tanh(v_2); \dots; \tanh(v_n)] \in \mathbb{R}^n$. Briefly speaking, the nominal control law \mathbf{f}_n exponentially stabilizes the nominal dynamics (i.e. (1a) with nominal parameters and no disturbance d_t) while the robust control law \mathbf{f}_r mitigates the gap between the nominal and actual dynamics.

3.3.2 Rotational dynamics Similar to the controller design for the translational dynamics, we take error variables first in designing a controller for the rotational counterpart as follows:

$$\begin{aligned} \mathbf{e}_R &= \frac{1}{2}(\mathbf{R}^\top \mathbf{R}_d - \mathbf{R}_d^\top \mathbf{R})^\vee, & \mathbf{e}_\omega &= \mathbf{R}^\top \mathbf{R}_d \boldsymbol{\omega}_d - \boldsymbol{\omega} \\ \mathbf{e}_{r1} &= \mathbf{e}_\omega + \Lambda_r \mathbf{e}_R, & \mathbf{e}_{r2} &= \dot{\mathbf{e}}_{r1} + \mathbf{e}_{r1}, & \mathbf{e}_r &= [\mathbf{e}_R; \mathbf{e}_{r1}; \mathbf{e}_{r2}] \end{aligned} \quad (7)$$

The error variables for the orientation \mathbf{e}_R and the angular velocity \mathbf{e}_ω are defined following Lee et al. (2010) where $\mathbf{R}_d \in \text{SO}(3)$ and $\boldsymbol{\omega}_d \in \mathbb{R}^3$ are the desired orientation and body angular velocity, respectively. $\Lambda_r \in \mathbb{R}_{>0}^{3 \times 3}$ is a diagonal control gain. Then, the proposed gRITE control law for the rotational dynamics is as follows:

$$\boldsymbol{\tau} = \boldsymbol{\tau}_n + \boldsymbol{\tau}_r \quad (8a)$$

$$\begin{aligned} \boldsymbol{\tau}_n &= \boldsymbol{\omega}^\wedge \bar{\mathbf{J}}_b \boldsymbol{\omega} - \bar{\mathbf{J}}_b (\boldsymbol{\omega}^\wedge \mathbf{R}^\top \mathbf{R}_d \boldsymbol{\omega}_d - \mathbf{R}^\top \mathbf{R}_d \dot{\boldsymbol{\omega}}_d) + \\ &\quad \bar{\mathbf{J}}_b \mathbf{K}_{rp} \mathbf{e}_R + \bar{\mathbf{J}}_b \mathbf{K}_{rd} \mathbf{e}_\omega \end{aligned} \quad (8b)$$

$$\begin{aligned} \boldsymbol{\tau}_r &= (\mathbf{K}_{ri} + \rho_r \mathbf{I}_3)(\mathbf{e}_{r1}(t) - \mathbf{e}_{r1}(0)) + \\ &\quad \int_0^t (\mathbf{K}_{ri} + \rho_r \mathbf{I}_3)\mathbf{e}_{r1}(\tau) + \boldsymbol{\Gamma}_r \text{Tanh}(\boldsymbol{\Theta}_r \mathbf{e}_{r1}(\tau)) d\tau \end{aligned} \quad (8c)$$

$\mathbf{K}_{rp}, \mathbf{K}_{rd}, \mathbf{K}_{ri}, \boldsymbol{\Gamma}_r, \boldsymbol{\Theta}_r \in \mathbb{R}_{>0}^{3 \times 3}$ and $\rho_r \in \mathbb{R}_{>0}$ are diagonal control gains, and the nominal control law $\boldsymbol{\tau}_n$ exponentially stabilizes the nominal error dynamics where the nominal moment of inertia $\bar{\mathbf{J}}_b$ is considered and no disturbance d_r exists Lee et al. (2010).

4 Stability analysis

Using the derived control laws for the translational and rotational dynamics (6), (8), we analyze stability of each closed-loop system. Note that the following analysis is motivated by Xian and Zhang (2016). We assume the boundedness of external disturbance and its time-derivatives as in other papers Kim et al. (2017); Lee et al. (2022); Hua et al. (2021):

Assumption 1. $d_t, \dot{d}_t, d_r, \dot{d}_r$ are continuously differentiable and bounded, and \ddot{d}_t, \ddot{d}_r are bounded.

4.1 Translational dynamics

From (1a), (6), dynamics of e_{t2} can be written as

$$m\dot{e}_{t2} = \mathbf{N}_t - \mathbf{K}_{ti}e_{t2} - \Gamma_t \text{Tanh}(\Theta_t e_{t1}) - e_{t1} \quad (9)$$

where

$$\mathbf{N}_t = (m - \bar{m})\ddot{\mathbf{p}}_d - \dot{d}_t - \bar{m}(\mathbf{K}_{tp}\dot{\mathbf{e}}_p + \mathbf{K}_{td}\ddot{\mathbf{e}}_p) + e_{t1}$$

$$\mathbf{N}_{td} = (m - \bar{m})\ddot{\mathbf{p}}_d - \dot{d}_t.$$

Define $\tilde{\mathbf{N}}_t = \mathbf{N}_t - \mathbf{N}_{td} = -\bar{m}(\mathbf{K}_{tp}\dot{\mathbf{e}}_p + \mathbf{K}_{td}\ddot{\mathbf{e}}_p) + e_{t1}$, then there exist a constant $\mu_t > 0$ satsifying

$$\|\tilde{\mathbf{N}}_t\| \leq \mu_t \|e_t\|. \quad (10)$$

Now, we define a Lyapunov candidate function V_t as

$$V_t = \frac{1}{2}\mathbf{e}_p^\top \mathbf{e}_p + \frac{1}{2}\mathbf{e}_{t1}^\top \mathbf{e}_{t1} + \frac{1}{2}m\mathbf{e}_{t2}^\top \mathbf{e}_{t2} + Q_t(t) \quad (11)$$

where

$$Q_t = \sum_{i=1}^n \frac{\Gamma_{t,i}}{\Theta_{t,i}} \ln(\cosh(\Theta_{t,i} e_{t1,i})) - e_{t1,i} N_{td,i} + \frac{\Gamma_{t,i}}{\Theta_{t,i}} \ln 2.$$

For the ease of analysis, here we also derive the time-derivative of V_t as

$$\begin{aligned} \dot{V}_t = & -\mathbf{e}_p^\top \mathbf{\Lambda}_t \mathbf{e}_p - \|e_{t1}\|^2 - \mathbf{e}_{t2}^\top (\mathbf{K}_{ti} + \rho_t \mathbf{I}_3) \mathbf{e}_{t2} + \\ & \mathbf{e}_p^\top \mathbf{e}_{t1} + \mathbf{e}_{t2}^\top \tilde{\mathbf{N}}_t + O_t(t) \end{aligned}$$

where $O_t = \mathbf{e}_{t1}^\top (\mathbf{N}_{td} - \dot{\mathbf{N}}_{td}) - \mathbf{e}_{t1}^\top \Gamma_t \text{Tanh}(\Theta_t e_{t1})$.

Lemma 1. Take $\Gamma_{t,i} \geq \|N_{td,i}\|_\infty + \|\dot{N}_{td,i}\|_\infty \forall i$. Then, Q_t satisfies the following inequalities:

$$\begin{aligned} \sum_{i=1}^n (\Gamma_{t,i} - \|N_{td,i}\|_\infty) |e_{t1,i}| & \leq Q_t(t) \leq \\ \sum_{i=1}^n (\Gamma_{t,i} + \|N_{td,i}\|_\infty) |e_{t1,i}| + \frac{\Gamma_{t,i}}{\Theta_{t,i}} \ln 2. & \end{aligned}$$

Proof. Finite $\Gamma_{t,i}$ exists by the Assumption 1, and the inequalities can be derived by using the fact that $|x| \leq \ln(\cosh(x)) + \ln 2 = \ln(e^x + e^{-x})$ and $\ln(\cosh(x)) \leq |x|$ for any $x \in \mathbb{R}$.

Lemma 2. Take $\Gamma_{t,i} \geq \|N_{td,i}\|_\infty + \|\dot{N}_{td,i}\|_\infty \forall i$. Then, with $c = 0.2785$, the upper bound of O_t can be obtained as

$$O_t \leq \sum_{i=1}^n \Gamma_{t,i} |e_{t1,i}| (1 - \tanh(\Theta_{t,i} |e_{t1,i}|)) \leq \sum_{i=1}^n \frac{\Gamma_{t,i}}{\Theta_{t,i}} c.$$

Proof. Finite $\Gamma_{t,i}$ exists by Assumption 1, and the upper bound can be obtained by using the fact that $\max_{x \in \mathbb{R}} \{|x| - x \tanh(x)\} \leq c$ Polycarpou and Ioannou (1996); Jia et al. (2019) and the control gain condition on $\Gamma_{t,i}$.

Lemma 3. Assume that the following scalar differential equation holds for any sufficiently smooth $\alpha(\cdot) \in \mathcal{K}_\infty$ and constant scalar c_s :

$$\dot{s} \leq -\alpha(s) + \alpha(c_s).$$

Then, there exist $\beta(\cdot, \cdot) \in \mathcal{KL}$ such that the following holds:

$$s(t) \leq \beta(s(0) - c_s, t) + c_s \quad \forall t \geq 0.$$

Proof. See the proof in Appendix 8.2.

Before presenting the main analysis result, we define $\lambda_m(\mathbf{A}), \lambda_M(\mathbf{A})$ as minimum and maximum eigenvalues of a matrix $\mathbf{A} \in \mathbb{R}_{>0}^{n \times n}$.

Theorem 1. For control gains satisfying

$$\begin{aligned} \Gamma_{t,i} & \geq \|N_{td,i}\|_\infty + \|\dot{N}_{td,i}\|_\infty \quad \forall i \\ \lambda_m(\mathbf{\Lambda}_t) & \geq 0.5 \\ \eta_t^* & \geq \mu_t^2 / (2\lambda_m(\mathbf{K}_{ti})) \end{aligned}$$

where $\eta_t^* = \min\{\lambda_m(\mathbf{\Lambda}_t) - \frac{1}{2}, \frac{1}{2}, \rho_t\}$, the closed-loop system of the translational dynamics consisting of (5) and (9) is ultimately bounded, and the ultimate bound can be made arbitrarily small.

Proof. See the proof in Appendix 8.3.

Briefly speaking, to satisfy the control gain conditions, one should take large enough \mathbf{K}_{ti} and Γ_t . Furthermore, the steady-state error bound can be arbitrarily shrunk by taking large enough $\mathbf{\Lambda}_t$, and this corresponds to the fact that no steady-state error exists if the sign function is used instead of tanh Xian et al. (2004). However, as will be analyzed at the end of this section, the use of tanh instead of sign function has merits in terms of input chattering attenuation.

4.2 Rotational dynamics

From (1b) and (8), dynamics of e_{r2} can be obtained as

$$\begin{aligned} J_b \dot{e}_{r2} = & -(\mathbf{K}_{ri} + \rho_r \mathbf{I}_3) e_{r2} - \Gamma_r \text{Tanh}(\Theta_r e_{r1}) - \frac{1}{2} \dot{\mathbf{J}}_b e_{r2} \\ & - e_{r1} + \tilde{\mathbf{N}}_r + \mathbf{N}_{rd} \end{aligned} \quad (12)$$

where

$$\begin{aligned} \mathbf{N}_{rd} & = (\dot{\mathbf{E}} - \dot{\mathbf{E}}) - \dot{d}_r, \\ \tilde{\mathbf{N}}_r & = -\dot{\mathbf{J}}_b (\mathbf{K}_{rp} \mathbf{e}_R + \mathbf{K}_{rd} \mathbf{e}_\omega) - \bar{\mathbf{J}}_b (\mathbf{K}_{rp} \dot{\mathbf{e}}_R + \mathbf{K}_{rd} \dot{\mathbf{e}}_\omega) \\ & + e_{r1} + \frac{1}{2} \dot{\mathbf{J}}_b e_{r2} + (\mathbf{J}_b - \dot{\mathbf{J}}_b) \dot{e}_{r1} + \dot{\mathbf{J}}_b \mathbf{\Lambda}_r \mathbf{C} \mathbf{e}_\omega + \\ & \mathbf{J}_b \mathbf{\Lambda}_r (\dot{\mathbf{C}} \mathbf{e}_\omega + \mathbf{C} \dot{\mathbf{e}}_\omega), \\ \mathbf{E} & = \mathbf{J}_b (\mathbf{R}^\top \mathbf{R}_d \dot{\boldsymbol{\omega}}_d - \boldsymbol{\omega}^\wedge \mathbf{R}^\top \mathbf{R}_d \boldsymbol{\omega}_d), \\ \mathbf{C} & = \frac{1}{2} [\text{tr}(\mathbf{R}^\top \mathbf{R}_d) \mathbf{I}_3 - \mathbf{R}^\top \mathbf{R}_d]. \end{aligned}$$

Here, we use the fact that $\dot{\mathbf{e}}_R = \mathbf{C} \mathbf{e}_\omega$ where $\|\mathbf{C}\|_2 \leq 1$ for any $\mathbf{R}^\top \mathbf{R}_d \in \text{SO}(3)$, and $\dot{\mathbf{E}} = \mathbf{E}|_{\mathbf{J}_b = \bar{\mathbf{J}}_b}$. From Remark 3

in Xian et al. (2004), there exists $\mu_r(\cdot) \in \mathcal{K}_\infty$ such that $\|\tilde{N}_r\| \leq \mu_r(\|e_r\|)\|e_r\|$ holds.

Now, we define a Lyapunov candidate function V_r as

$$V_r = \frac{1}{2}e_{r1}^\top e_{r1} + \frac{1}{2}e_{r2}^\top J_b e_{r2} + Q_r + \Psi \quad (13)$$

where

$$\begin{aligned} Q_r &= \sum_{i=1}^n \frac{\Gamma_{r,i}}{\Theta_{r,i}} \ln(\cosh(\Theta_{r,i} e_{r1,i})) - e_{r1,i} N_{rd,i} + \frac{\Gamma_{r,i}}{\Theta_{r,i}} \ln 2 \\ \Psi &= \frac{1}{2} \text{tr}[\mathbf{I}_3 - \mathbf{R}^\top \mathbf{R}_d]. \end{aligned}$$

Note that to capture non-Euclidean property of $\text{SO}(3)$, Ψ is introduced in (13) instead of $e_p^\top e_p$ in (11).

Lemma 4. Assume that control gains satisfy the following:

$$\lambda_m(\mathbf{K}_{ri}) \geq \frac{1}{2\eta_r^*} \mu_r^2 \left(\sqrt{\frac{1}{\eta_r} \beta_r(|V_r(0) - \Xi_r|, t)} + \frac{\Xi_r}{\eta_r} \right)$$

$$\lambda_m(\Lambda_r) \geq 0.5$$

$$\Gamma_{r,i} \geq \|N_{rd,i}\|_\infty + \|\dot{N}_{rd,i}\|_\infty \quad \forall i$$

where $\eta_r^* = \min\{\lambda_m(\Lambda_r) - \frac{1}{2}, \frac{1}{2}, \rho_r\}$. If $\Psi(t) \leq \psi$ holds for some $0 < \psi < 2$ and $t \in [t_1, t_2]$ for any $0 \leq t_1 < t_2$, then the following holds for all $t \in [t_1, t_2]$:

$$\dot{V}_r \leq -\Omega_r(V_r) + \Omega_r(\Xi_r). \quad (14)$$

Here, $\beta_r(\cdot, \cdot) \in \mathcal{KL}$, and $\Xi_r = \chi(\sigma_r)$ for some $\chi(\cdot) \in \mathcal{K}_\infty$ and $\sigma_r = \sum \frac{\Gamma_{r,i}}{\Theta_{r,i}} \ln 2$ whose detailed definitions are in Appendix 8.4.

Proof. See the proof in Appendix 8.4.

Theorem 2. Assume that control gains Θ_r, Γ_r are selected so that $\Xi_r < \psi$ holds for some $\psi \in (0, 2)$. We also assume that control gain conditions in Lemma 2 hold, and the initial condition satisfies

$$V_r(0) \leq \psi - \epsilon_\psi \quad (15)$$

for arbitrarily small positive scalar ϵ_ψ . Then, the closed-loop system of the rotational dynamics consisting of (1b) and (8) is ultimately bounded, and the ultimate bound can be made arbitrarily small.

Proof. See the proof in Appendix 8.5.

Although the sign function can provide additional merit of asymptotic stability Gu et al. (2022); Xian et al. (2004) if used instead of the tanh function in the control law (6), (8), it may result in input chattering. Considering the omnidirectional aerial robot where some actuators (i.e. servomotors) show unknown, non-negligible time delay in tracking the input command, such input chattering can deteriorate the tracking performance. The tanh function in the proposed control law relieves this problem by providing sufficient smoothness in the control input while endowing the necessary disturbance attenuation property with moderately high control gains of Θ_t, Θ_r .

As done in Xian and Zhang (2016), gRITE control only with the robust control law f_r and τ_r can provide the

same property of boundedness with arbitrary small bound in theory. However, since the robust control law does not exploit the structure of the system dynamics, feedforward terms such as gravity $\bar{m}g\mathbf{R}^\top b_3$ in (6b) and centrifugal force $\omega^\wedge \bar{J}_b \omega$ in (8b) cannot be utilized, and this may degrade initial transient performance. Furthermore, since proportional and derivative gains for position/orientation errors e_p, e_R cannot be tuned independently to the integral gains, the gain tuning process can become demanding. The nominal control law mitigates the two problems because it is designed to involve feedforward terms and has proportional, derivative gains independent to the integral gains.

5 Whole-body motion planning

This section overviews our whole-body trajectory generation algorithm designed for an OAM whose objective can be summarized as the following statement:

Whole-body Motion Planning For the given goal pose of the end-effector, find a whole-body motion trajectory of the OAM (i.e. pose of the floating base and joint angles of the robotic arm) that utilizes the entire configuration space $\mathcal{C} = \mathbb{R}^3 \times \text{SO}(3) \times \mathbb{R}^n$ and is free from self-collision and avoid obstacles while enforcing the end-effector to reach the goal.

We utilize both offline and online planning to enhance convergence to the predefined end-effector goal pose and to enable reactive real-time replanning with respect to potential disturbance. This allows the OAM to reach the predefined end-effector goal pose and refine the entire state trajectory in real time. In the initial stage, our algorithm focuses on the end-effector trajectory. The end-effector pose is modeled as a particle in a 3D Euclidean space with orientation. As a result, the globally optimal, collision-free end-effector pose trajectory can be obtained within a few seconds even under a setting where the problem is highly nonlinear due to the rotational motion, and the trajectory horizon is longer than 10 s. Then, our algorithm proceeds to local online whole-body motion planning. Here, the primary consideration is to consider the whole-body motion while tracking the previously determined optimal end-effector pose trajectory. Before presenting algorithmic details, we define notations and enumerate assumptions used for our whole-body motion planner.

Let us denote the end-effector position and orientation as ${}^E\mathbf{p} \in \mathbb{R}^3$ and ${}^E\mathbf{R} \in \text{SO}(3)$, respectively, where the left-superscript E stands for the end-effector. These quantities will be used with right-subscripts d and g which indicate ‘desired’ and ‘goal’ values. The desired end-effector linear and body angular velocities are represented as ${}^E\mathbf{v}_d$ and ${}^E\boldsymbol{\omega}_d$. The set of all points in \mathbb{R}^3 constructing the i^{th} obstacle among the N_o obstacles is denoted as \mathcal{O}_i . Lastly, we define $\boldsymbol{\theta} \in \mathbb{R}^n$ to be the joint angles of the robotic arm.

Assumption 2. All obstacles are static, known, and modeled as composites of multiple ellipsoids.

Only for notational simplicity, we describe an obstacle with a single ellipsoid from the following. That is,

$$\begin{aligned} \mathcal{O}_i &= \mathcal{E}(\bar{\mathbf{p}}_i, \bar{\mathbf{Q}}_i) \subset \mathbb{R}^3 \\ \mathcal{E}(\bar{\mathbf{p}}_i, \bar{\mathbf{Q}}_i) &:= \{\mathbf{p} \in \mathbb{R}^3 | (\mathbf{p} - \bar{\mathbf{p}}_i)^\top \bar{\mathbf{Q}}_i^{-1} (\mathbf{p} - \bar{\mathbf{p}}_i) \leq 1\} \end{aligned}$$

where $\bar{\mathbf{p}}_i \in \mathbb{R}^3$ and $\bar{\mathbf{Q}}_i \in \mathbb{R}_{>0}^{3 \times 3}$ denote the center and the shape matrix of the i^{th} ellipsoid, respectively. This assumption allows us to formulate collision avoidance constraints with obstacles using finite dimensional parameters of $\bar{\mathbf{p}}_i$ and $\bar{\mathbf{Q}}_i$. When it is difficult to represent a particular obstacle as a single ellipsoid, we can construct a composite of multiple ellipsoids that fully encompass the obstacle.

Assumption 3. There exists at least one curve in $\mathcal{OBS}^c \subset \mathbb{R}^3$ starting from any points in \mathcal{OBS}^c to the goal position in \mathcal{OBS}^c where the set \mathcal{OBS} is defined as $\mathcal{OBS} = \bigcup_{i=1}^{N_o} \mathcal{O}_i$.

The last assumption can be interpreted as the goal not being positioned within a fully obstructed region enclosed by obstacles. This is to ensure existence of a path from any initial position to the goal position of the end-effector. With these assumptions, we can formulate the following Optimal Control Problems (OCPs) for our cascaded whole-body motion planner.

5.1 Offline end-effector trajectory generation

From Assumption 2, it becomes apparent that the end-effector trajectory avoids collisions with obstacles if and only if the following inequalities are satisfied:

$$\begin{aligned} h_i({}^E\mathbf{p}_d(k)) &> 0 \quad \forall i, k \\ h_i({}^E\mathbf{p}_d) := ({}^E\mathbf{p}_d - \bar{\mathbf{p}}_i)^T \bar{\mathbf{Q}}_i^{-1} ({}^E\mathbf{p}_d - \bar{\mathbf{p}}_i) - 1 \end{aligned}$$

where k denotes the discretized time index throughout this section. However, directly incorporating these constraints into discrete-time OCPs may lead to a numerical issue of generating an optimal trajectory that penetrates very thin ellipsoids within a single time interval. In such cases, the system may collide with ellipsoids although the optimized trajectory is feasible. Therefore, instead, we formulate the following collision avoidance constraints, which impose constraints on the linear velocity.

$$\begin{aligned} \tilde{h}_i({}^E\mathbf{p}_d(k), {}^E\mathbf{v}_d(k)) &> 0 \quad \forall i, k \\ \tilde{h}_i({}^E\mathbf{p}_d, {}^E\mathbf{v}_d) := \frac{\partial h_i}{\partial {}^E\mathbf{p}_d}({}^E\mathbf{p}_d) {}^E\mathbf{v}_d + \gamma_i(h_i({}^E\mathbf{p}_d)) \end{aligned} \quad (16)$$

where $\gamma_i(\cdot) \in \mathcal{K}_\infty$ can be chosen arbitrarily. We designed γ_i as linear functions for simplicity. Provided that the inequalities (16) and $h_i({}^E\mathbf{p}_d(0)) > 0$ hold, the forward invariance of $h_i > 0$ is guaranteed by the comparison lemma (Khalil and Grizzle 2002, Lemma 3.4).

The modified collision avoidance constraints (16) rely only on the optimization variables in the translational motion. Thus, we can construct the following decoupled jerk minimization problem.

$$\begin{aligned} \min_{{}^E\mathbf{x}_p, {}^E\ddot{\mathbf{v}}_d} \sum_{k=0}^{N_T-1} \|{}^E\ddot{\mathbf{v}}_d(k)\|_{R_v}^2 \\ \text{s.t. } {}^E\mathbf{x}_p(0) = [{}^E\mathbf{p}(0); \mathbf{0}; \mathbf{0}] \\ {}^E\mathbf{x}_p(N_T) = [{}^E\mathbf{p}_g; \mathbf{0}; \mathbf{0}] \\ \forall_k \quad {}^E\mathbf{x}_p(k+1) = {}^E\mathbf{f}_p({}^E\mathbf{x}_p(k), {}^E\ddot{\mathbf{v}}_d(k)) \\ \forall_{i,k} \quad \tilde{h}_i({}^E\mathbf{p}_d(k), {}^E\mathbf{v}_d(k)) > 0 \end{aligned} \quad (17)$$

$$\begin{aligned} \min_{{}^E\mathbf{x}_R, {}^E\ddot{\omega}_d} \sum_{k=0}^{N_T-1} \|{}^E\ddot{\omega}_d(k)\|_{R_\omega}^2 \\ \text{s.t. } {}^E\mathbf{x}_R(0) = ({}^E\mathbf{R}(0), \mathbf{0}, \mathbf{0}) \\ {}^E\mathbf{x}_R(N_T) = ({}^E\mathbf{R}_g, \mathbf{0}, \mathbf{0}) \\ \forall_k \quad {}^E\mathbf{x}_R(k+1) = {}^E\mathbf{f}_R({}^E\mathbf{x}_R(k), {}^E\ddot{\omega}_d(k)) \end{aligned} \quad (18)$$

Here, ${}^E\mathbf{x}_p := [{}^E\mathbf{p}_d; {}^E\mathbf{v}_d; {}^E\dot{\mathbf{v}}_d] \in \mathbb{R}^9$, ${}^E\mathbf{x}_R := ({}^E\mathbf{R}_d, {}^E\omega_d, {}^E\dot{\omega}_d) \in \text{SO}(3) \times \mathbb{R}^6$, and $N_T = T_f/\Delta t$. T_f and Δt are user-defined desired reaching time and time discretization. ${}^E\mathbf{f}_p$ and ${}^E\mathbf{f}_R$ are time-discretized linear and nonlinear kinematics of the translational and rotational motion. The detailed definitions of ${}^E\mathbf{f}_p$ and ${}^E\mathbf{f}_R$ can be found in Appendix 8.6. \mathbf{R}_v and \mathbf{R}_ω are positive definite weight matrices. ${}^E\mathbf{p}(0)$ and ${}^E\mathbf{R}(0)$ are obtained from the forward kinematics with the measured values of $\mathbf{p}(0)$, $\mathbf{R}(0)$, and $\theta(0)$ when the planner algorithm initiates. It is worth noting that, if the objective is only related to the goal position, (18) can be omitted thanks to the fact that (17) and (18) are decoupled.

5.2 Online whole-body motion planning

Unlike the offline end-effector trajectory generation, whole-body motion planning necessitates the consideration of collision avoidance among rigid bodies, identification of the optimal configuration among those achieving the same end-effector pose, and online replanning to react to uncertainties and refine the end-effector trajectory if unavoidable. This subsection provides details of how each of these considerations is incorporated into the OCP.

5.2.1 Collision avoidance constraint Let us define the i^{th} ellipsoid $\mathcal{A}_i(t)$ comprising the aerial manipulator at time t as

$$\begin{aligned} \mathcal{A}_i(t) &:= \mathcal{E}({}^A\bar{\mathbf{p}}_i(t), {}^A\bar{\mathbf{Q}}_i(t)) \\ {}^A\bar{\mathbf{Q}}_i(t) &:= {}^A\mathbf{R}_i(t)^T {}^A\bar{\mathbf{Q}}_i(0) {}^A\mathbf{R}_i(t) \end{aligned}$$

In the above, ${}^A\bar{\mathbf{p}}_i$ and ${}^A\mathbf{R}_i$ represents the position and orientation of the i^{th} link obtained through the forward kinematics, where the multirotor base corresponds to $i = 0$. ${}^A\bar{\mathbf{Q}}_i(0)$ is the shape matrix calculated at ${}^A\mathbf{R}_i = \mathbf{I}_3$.

When obstacles and robot components are all modeled with ellipsoids, collision avoidance can be ensured if there is no intersection between each pair of robot and obstacle ellipsoids. Let us consider a set generated by the Minkowski sum of two sets of ellipsoids as $\bar{\mathcal{B}} = \mathcal{B}_1 \oplus (-\mathcal{B}_2)$. The condition for the absence of intersection between the two ellipsoids can be expressed as $0 \notin \bar{\mathcal{B}}$. However, in general, $\bar{\mathcal{B}}$ is not an ellipsoid. To resolve this, similar to the work done in Son et al. (2020) where the most compact ellipsoid is used that encompasses $\bar{\mathcal{B}}$ through trace minimization, we can guarantee the absence of intersection between the given two ellipsoids if the following condition is satisfied Seo et al. (2019).

$$\begin{aligned} \hat{h}(\mathcal{B}_1, \mathcal{B}_2) &> 0 \\ \hat{h}(\mathcal{B}_1, \mathcal{B}_2) &:= (\bar{\mathbf{p}}_{\mathcal{B}_1} - \bar{\mathbf{p}}_{\mathcal{B}_2})^T \bar{\mathbf{Q}}^{-1}(\mathcal{B}_1, \mathcal{B}_2)(\bar{\mathbf{p}}_{\mathcal{B}_1} - \bar{\mathbf{p}}_{\mathcal{B}_2}) - 1 \\ \bar{\mathbf{Q}}(\mathcal{B}_1, \mathcal{B}_2) &:= \sum_{i=1}^2 \sum_{j=1}^2 \frac{\bar{\mathbf{Q}}_{\mathcal{B}_i}}{\sqrt{\text{tr}(\bar{\mathbf{Q}}_{\mathcal{B}_i})}} \sqrt{\text{tr}(\bar{\mathbf{Q}}_{\mathcal{B}_j})} \end{aligned} \quad (19)$$

Hence, the collision avoidance is guaranteed if (19) holds for all pairs of ellipsoids of robots and obstacles for all $t \geq 0$.

5.2.2 Cost function In comparison with ground robot-based mobile manipulators, aerial manipulators are more susceptible to disturbance caused by interaction forces between the end-effector and the target object during manipulation. To mitigate this, it is imperative to secure the manipulability of the robot arm. Consequently, we incorporate the following manipulability index into our cost function:

$$\phi_m(\boldsymbol{\theta}) := \mu_v \det(\mathbf{J}_v(\boldsymbol{\theta})\mathbf{J}_v^\top(\boldsymbol{\theta})) + \mu_\omega \det(\mathbf{J}_\omega(\boldsymbol{\theta})\mathbf{J}_\omega^\top(\boldsymbol{\theta})) \quad (20)$$

Here, \mathbf{J}_v and \mathbf{J}_ω are Jacobian matrices of relative position and orientation of the end-effector with respect to the multirotor base. μ_v and μ_ω are positive weights. A higher value of ϕ_m indicates greater manipulability, signifying that the robot arm configuration is positioned farther away from singularity Lynch and Park (2017). Finally, denoting $\mathbf{x}_d := (\mathbf{p}_d, \mathbf{R}_d, \boldsymbol{\theta}_d) \in \mathbb{R}^3 \times \text{SO}(3) \times \mathbb{R}^n$, ${}^E\mathbf{x}_d := ({}^E\mathbf{p}_d, {}^E\mathbf{R}_d) \in \mathbb{R}^3 \times \text{SO}(3)$ and $\mathbf{u}_d := [\mathbf{v}_d; \boldsymbol{\omega}_d; \dot{\boldsymbol{\theta}}_d] \in \mathbb{R}^{6+n}$, we design the following state cost ϕ_x and input cost ϕ_u

$$\begin{aligned} \phi_x(\mathbf{x}_d, {}^E\mathbf{x}_d) &:= \|{}^E\mathbf{p}(\mathbf{x}_d) - {}^E\mathbf{p}_d\|_{\mathbf{Q}_p}^2 - \phi_m(\boldsymbol{\theta}_d) \\ &\quad + \text{tr}(\mathbf{Q}_R(\mathbf{I}_3 - {}^E\mathbf{R}_d^\top {}^E\mathbf{R}(\mathbf{x}_d))) \quad (21) \\ \phi_u(\mathbf{u}_d) &:= \|\mathbf{u}_d\|_{\mathbf{R}_u}^2, \end{aligned}$$

where \mathbf{Q}_p , \mathbf{Q}_R and \mathbf{R}_u are all positive definite weight matrices. ${}^E\mathbf{p}(\mathbf{x}_d)$ and ${}^E\mathbf{R}(\mathbf{x}_d)$ are computed by forward kinematics using \mathbf{x}_d .

5.2.3 Kinematics-level nonlinear model predictive control With the obstacle avoidance constraints (19) and the cost functions (21), we formulate and solve the following OCP at each replanning interval, employing a nonlinear model predictive control (NMPC) approach:

$$\begin{aligned} \min_{\mathbf{x}_d, \mathbf{u}_d} & \phi_x(\mathbf{x}_d(N_H), {}^E\mathbf{x}_d(N_H)) \\ & + \sum_{k=0}^{N_H-1} \phi_x(\mathbf{x}_d(k), {}^E\mathbf{x}_d(k)) + \phi_u(\mathbf{u}_d(k)) \\ \text{s.t. } & \mathbf{x}_d(0) = (\mathbf{p}, \mathbf{R}, \boldsymbol{\theta}) \quad (22) \\ \forall_k & \mathbf{x}_d(k+1) = \mathbf{f}_x(\mathbf{x}_d(k), \mathbf{u}_d(k)) \\ \forall_k & \mathbf{u}_m \preceq \mathbf{u}_d(k) \preceq \mathbf{u}_M \\ \forall_k & \mathbf{A}_\theta \boldsymbol{\theta}_d(k) \preceq \mathbf{b}_\theta \\ \forall_{i,j,k} & \hat{h}(\mathcal{A}_i(k), \mathcal{O}_j) > 0 \end{aligned}$$

Here, \mathbf{p} , \mathbf{R} and $\boldsymbol{\theta}$ are the measured values at every replanning time. \mathbf{f}_x represents discretized kinematic relations for the position, rotation matrix, and joint angle. See Appendix 8.7 for the detail. The upper and lower bounds for input \mathbf{u}_d are denoted as \mathbf{u}_M and \mathbf{u}_m . The fourth inequality constraint, i.e. $\mathbf{A}_\theta \boldsymbol{\theta}_d(k) \preceq \mathbf{b}_\theta$, prevents self-collision between the manipulator and the multirotor base, where \preceq denotes element-wise inequality. The horizon length is denoted as N_H . After solving the optimization problem (22) and refining the whole-body trajectory, we utilize \mathbf{p}_d , \mathbf{v}_d , \mathbf{R}_d , and $\boldsymbol{\omega}_d$ as desired values for the controller in (6) and (8). Simultaneously, $\boldsymbol{\theta}_d$ and $\dot{\boldsymbol{\theta}}_d$ serve as desired values for the external robot arm controller.

Table 2. Main components of the system

Component	Product name	Quantity
Onboard computer	Intel NUC i3	1
Rotor	Armatan Oomph TITAN 2306/2450KV	6
Propeller	APC BD6x4.2E-3-B4	6
Servo (base)	Dynamixel XC330 series	6
Servo (manipulator)	Dynamixel XM430 & XC330 series	4
ESC	Hobbywing XRotor Micro 40A 4in1	2
PWM generator	Nucleo F446RE	1
IMU sensor	Vectornav VN-100	1
Battery	Turnigy 4200 mAh 4S LiPo	1

In scenarios where the manipulator is constrained to planar motion, the manipulability index ϕ_m in (20) becomes 0 as \mathbf{J}_v and \mathbf{J}_ω are not full rank. In such instances, ϕ_m can be computed utilizing the Jacobian matrices projected onto the plane of motion. Moreover, if the manipulator comprises solely revolute joints rotating in the same direction, the term associated with \mathbf{J}_ω remains constant and can be excluded from the cost function. For the case when the goal end-effector orientation is deemed inconsequential and omitted to be solved in (18), excluding the term $\text{tr}(\mathbf{Q}_R(\mathbf{I}_3 - {}^E\mathbf{R}_d^\top {}^E\mathbf{R}(\mathbf{x}_d)))$ in (21) suffices. This is because the remaining state cost also contains all of the state variable \mathbf{x}_d .

6 Experimental results

6.1 Setup

We construct a customized omnidirectional aerial manipulator whose CAD model can be found in Fig. 2. Table 2 lists main components of the platform whose net weight is about 2.13 kg. The manipulator is composed of 4 revolute joints where the first three joints rotate in the same direction while the last joint is for a gripper. Algorithms including the proposed controller, planner, and state estimator run in an onboard computer where we use Robot Operating System (ROS) in Ubuntu 20.04. The current state of the robot is estimated by a state estimation algorithm Kim (2023) which executes sensor fusion for measurements from Optitrack motion capture system and inertial measurement unit (IMU). The overall algorithm for hardware experiments is visualized in Fig. 3.

Three experiments are conducted. In the first experiment, we show the performance of the proposed controller by comparing the result that is obtained with the baseline controller, i.e. geometric PID Goodarzi et al. (2013). The objective is to regulate the pose of the multirotor base in the presence of the robotic arm's motion, and better regulation performance can be observed with the proposed control law. The second and third experiments are to demonstrate the proposed framework in one precise manipulation task of grasping-and-pulling an object. We consider two different environment settings: grasping-and-pulling an object 1) on the ground and 2) on a table. Compared to a conventional aerial manipulator based on an underactuated multirotor base inheriting a limited workspace, the omnidirectional aerial manipulator equipped with the proposed framework could accomplish the task in both environments by leveraging omnidirectionality and the extended workspace.

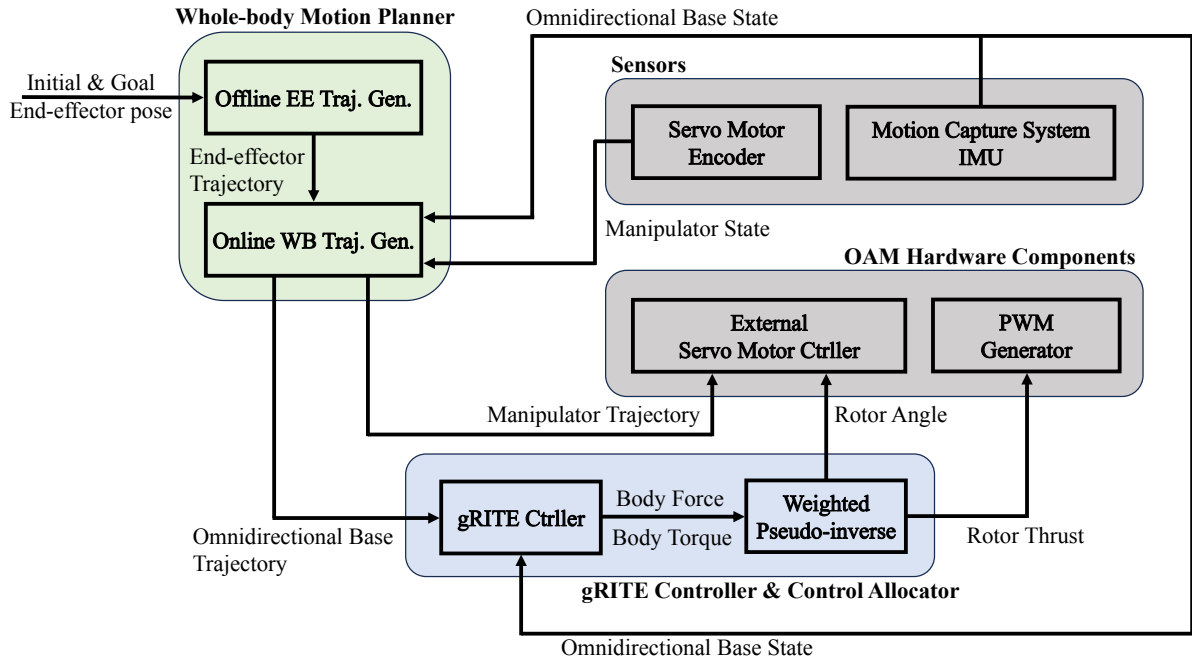


Figure 3. Overall algorithm flow for hardware experiments. EE and WB stand for End-effector and Whole-body, respectively.

Table 3. Controller and control allocation parameters (diagonal elements for matrices)

Controller			
Parameter	Value	Parameter	Value
\bar{m} [kg]	2.13	\bar{J}_b [kgm ²]	(0.02, 0.025, 0.035)
K_{tp}	(8, 8, 8)	K_{rp}	(15, 20, 10)
K_{td}	(5, 5, 5)	K_{rd}	(10, 9, 5)
K_{ti}	(2, 2, 4)	K_{ri}	(0.08, 0.08, 0.08)
Λ_t	(3, 2, 2)	Λ_r	(8, 8, 8)
Γ_t	(2, 2, 2)	Γ_r	(0.2, 0.2, 0.2)
Θ_t	(3, 3, 3)	Θ_r	(10, 10, 10)
ρ_t	1	ρ_r	0.02

Allocation	
Parameter	Value
W	(1, 1, 0.6, 0.6, 1, 1, 1, 1, 0.6, 0.6, 1, 1)

Table 4. Planner parameters and numerical integration method (block diagonal matrices for R_u)

Offline			
Parameter	Value	Parameter	Value
R_v, R_ω	I_3	γ_i	3
T_f [sec]	15	Δt [sec]	0.1

Online			
Parameter	Value	Parameter	Value
μ_v	0.01	μ_ω	—
Q_p	$5I_3$	R_u	(0.01 I_3 , 0.01 I_3 , 0.1 I_3)
Q_R	$4I_3$	$u_M, -u_m$	[I_3 ; 0.5 πI_3 ; 0.25 πI_3]
N_H	15	Δt [sec]	0.1

Numerical integration			
Parameter	Method	Parameter	Method
$E f_p, E f_R$	RK4	f_x	Euler

$$I_3 := [1; 1; 1]$$

6.2 Implementation details

Control gains we used during the whole experiments are listed in Table 3. In the gain tuning process, we first tune PID gains $K_{tp}, K_{td}, K_{ti}, K_{rp}, K_{rd}, K_{ri}$ while setting all the other gains to be zero. After finding proper PID gains, we freeze the PID gains and tune the other gains related to the integral of the tanh of the error, which are $\Lambda_t, \Gamma_t, \Theta_t, \rho_t, \Lambda_r, \Gamma_r, \Theta_r, \rho_r$. We first set ρ_t, Γ_t and ρ_r, Γ_r to be the same scale as K_{ti} and K_{ri} , respectively, and adjust them afterwards. Similarly, we initially take Λ_t, Λ_r to be slightly larger than 1 as they indicate the decay rate and tune them afterwards. Lastly, we initially set Θ_t, Θ_r to be 1 and increase them until achieving sufficient performance in disturbance rejection since larger Θ_t, Θ_r are analyzed to be effective in reducing the error bound.

We empirically find that the 2nd and 5th rotors depicted in Fig. 2 go near saturation when the robot hovers at 90° pitch angle with the identity weight matrix W in control allocation. This is because when hovering at 90° pitch angle, 1) the pseudo-inverse solution finds the minimum norm solution and 2) other rotors are less effective in compensating gravity as they are tilted with respect to the gravity direction. Considering the robotic arm configuration in Fig. 2, manipulation while maintaining non-zero or even 90° pitch angle can frequently occur during experiments. To relieve this issue, we allocate values smaller than 1 to the elements related to the 2nd and 5th rotors in the weight matrix W in (3). The value we use during all experiments can be found in Table 3.

Our experiments involve grasping a target object. Thus, a certain criterion is needed to determine whether the object is firmly grasped or not. For the criterion, we choose the current of the gripper servomotor. Before the experiments, the threshold for successful grasping is determined by securing various test objects with the gripper and observing the required value for it. In actual experiments, a low-pass filter is applied to the gripper servomotor's current. If the

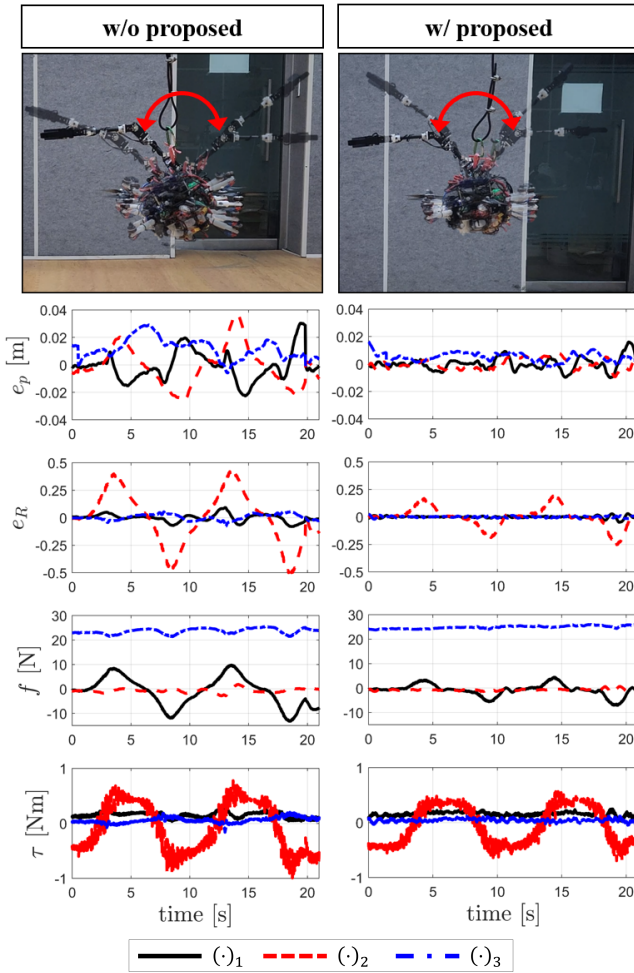


Figure 4. Results of setting 1 of Experiment 1: pose regulation at 0° pitch angle.

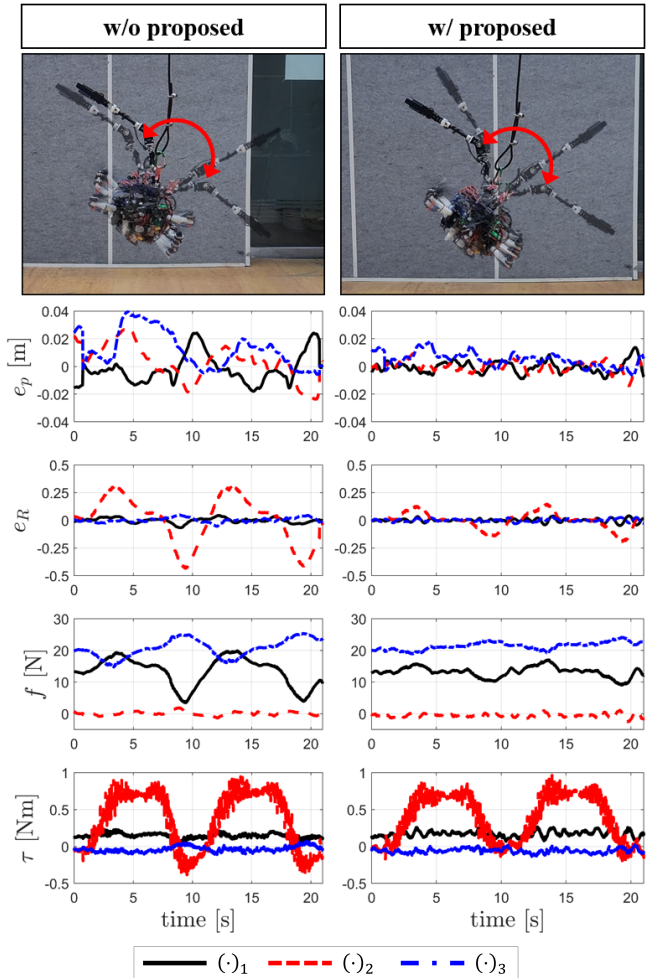


Figure 5. Results of setting 2 of Experiment 1: pose regulation at -30° pitch angle.

filtered value surpasses the pre-determined threshold after 1.5 seconds, the grasping is considered successful, and a new trajectory is planned for the subsequent mission, which is pulling. The command to grasp is given when the position error between the end-effector and the goal is less than 3 cm. If the criterion is not met after the command, the gripper is reopened. This process is repeated until successful grasping occurs.

The collision avoidance with the ground is efficiently addressed by representing both the base and individual links of the OAM as spheres. This pragmatic simplification allows us to express the constraint in the form of $r_i \leq z_i(t)$ where r_i is the radius and z_i is the height of the i^{th} component of the OAM. For OCPs described in (17), (18), and (22), we employed the open-source tool CasADi Andersson et al. (2019). The chosen nonlinear optimization solver was IPOPT with HSL libraries HSL (2007) serving as a linear solver. With this setup, the entire offline OCPs in (17) and (18) are solved within 3-5 seconds. The parameters used for our whole-body motion planner algorithm are shown in Table 4. Our OAM's revolute joints related to the motion of the manipulator rotate along the same direction, meaning that J_ω becomes constant. Thus, in the table, the value of μ_ω is not listed.

6.3 Experiment 1: controller comparison

The first experiment is to show effectiveness of the proposed controller in the presence of disturbance. We compared the proposed controller with a nonlinear PID controller Goodarzi et al. (2013); Su et al. (2023). The gains of the controller in comparison are sufficiently tuned until stable hovering is obtained at multiple non-zero pitch angles. For fair comparison, we set the corresponding PID gains of the proposed controller to be the same as the gains for the comparing controller. The gains can be found in Table 3.

The experiment is carried out in two different settings: pose regulation at 0° pitch angle and -30° pitch angle. We intentionally oscillate the manipulator to provide external disturbance to the multirotor base. In all settings, only the first and second joints of the manipulator are commanded to move from -45° to 45° with a period of 10 s. The results for 0° pitch angle and -30° pitch angle are illustrated in Figs. 4 and 5, respectively. In both figures, the above composite images show the motions of the manipulator and the multirotor base, exhibiting the superior performance of the proposed controller. The below graphs in both figures display pose error e_p , e_R and body force and torque f , τ obtained during the experiments.

In both experiments, while the maximum error in the translational motion does not exceed 0.02 m in the results obtained with the proposed controller, that in the results

Table 5. NMPC computation time of Experiment 2 [ms]

	(a) ground-basic	(b) ground-yaw	(c) ground-pitch
min	5.23	4.80	6.18
max	12.0	12.2	15.9
avg.	8.50	8.42	10.7

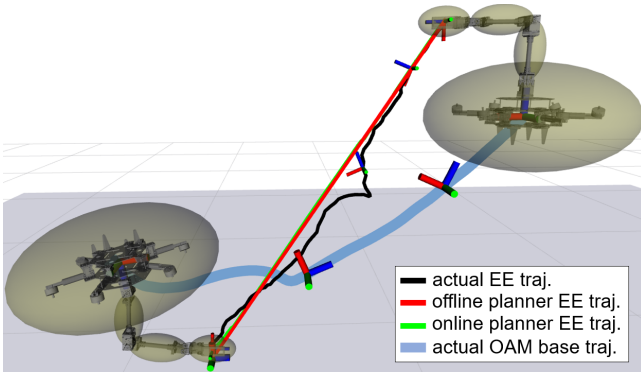


Figure 6. Visualization of trajectories computed by the whole-body motion planner in Experiment 2 setting (c) ground-pitch. The blue line indicates the motion of the multirotor base, and the red and green lines are end-effector trajectories computed by the offline and online planners. The black line is the actual trajectory traversed by the end-effector.

obtained without the proposed controller nearly reaches 0.04 m. The performance gap is more significant in the rotation direction which can be found in the second row of the graphs in Figs. 4 and 5. We presume that not the control law itself but the mechanical vibration of the manipulator and the resultant measurement noise in angular velocity are responsible for the jittering in τ_2 during all experiments with or without the proposed control law. This is because such jittering does not occur in any other control inputs, and we have experienced mechanical vibration due to backlash and clearance of servomotors which may be improved by fabricating the OAM using high-end servomotors.

6.4 Experiment 2: grasping-and-pulling an object on the ground

The second experiment is grasping-and-pulling an object on the ground which can hardly be conducted with a conventional aerial manipulator whose manipulator is attached on the top as the OAM in Fig. 1. We carry out three different scenarios which we call (a) ground-basic, (b) ground-yaw, and (c) ground-pitch. All scenarios and the data collected during the experiments are visualized in Fig. 7. Compared to (a) ground-basic, the initial orientation of the OAM in (b) ground-yaw is 180° rotated in the yaw direction. (c) ground-pitch starts with the same orientation as (a) ground-basic, but the target end-effector orientation is 180° rotated in the pitch direction.

We could confirm that the proposed whole-body motion planning algorithm can compute a collision-free and goal-reaching trajectory in all three scenarios having either different initial conditions or different target poses. For the ground-pitch scenario, we visualize the end-effector trajectory computed by the first-step offline planner (red), the whole-body trajectory generated by the second-step online planner (green) and the actual traversed end-effector

Table 6. NMPC computation time of Experiment 3 [ms]

	(a) table-far	(b) table-close
min	14.2	13.8
max	69.4	50.5
avg.	27.8	29.2

trajectory (black) in Fig. 6. Each ellipsoid represents each single rigid body comprising the OAM, used in deriving the collision avoidance constraints. We could also validate online replannability of the second-step NMPC-based planning algorithm in Table 5. The maximum computation time is less than 20 ms in all scenarios, indicating online replannability faster than 50 Hz.

The composite images at the top of Fig. 7 show the motion of the OAM during experiments. Position p and orientation q of the multirotor base and joint angles of the manipulator θ are visualized in the below graphs. As the multirotor rotates more than 90° pitch angle, we use quaternion $q = [q_w, q_x, q_y, q_z]$ in representing the orientation. Thanks to the omnidirectionality of the OAM platform and the capability of the proposed framework to address such merit in both planning and control, the mobile manipulator successfully performs precise manipulation while enjoying the extended workspace. As described in the composite images of Fig. 7, the three experiments demonstrate precise manipulation of grasping-and-pulling while maintaining the pitch angle over 90° and even near 180°.

6.5 Experiment 3: grasping-and-pulling an object on a table

The last experiment is to validate applicability of the proposed framework in a different setting of grasping-and-pulling an object on top of a table. The OAM should now additionally avoid collision with the table while accomplishing the task. Two different scenarios are considered: (a) table-far and (b) table-close. The results are summarized in Fig. 9. The proposed whole-body motion planner computes a trajectory so that the OAM simultaneously tilts the pitch angle and stretches the manipulator to satisfy both the collision avoidance constraint and the goal-reaching objective. It is noticeable that when the object on the table is far from the robot (i.e. scenario (a)), to ensure safety, the proposed whole-body motion planner computes a trajectory not only to tilt the pitch angle and stretch the manipulator but also to stay above the table. Although a non-negligible ground effect from the table exists while the OAM being above the table in scenario (a), sufficient tracking performance to accomplish the precise manipulation task can be achieved with the proposed controller.

The computation time taken for solving the second step NMPC is listed in Table 6. As an additional object to avoid exists compared to the Experiment 2, a little longer computation time is required, but still about 100 Hz on average is obtained, which is sufficient for online replanning. Trajectories computed from the offline and online planning algorithms and the actual traversed trajectory are visualized in Fig. 8 for scenario (a).

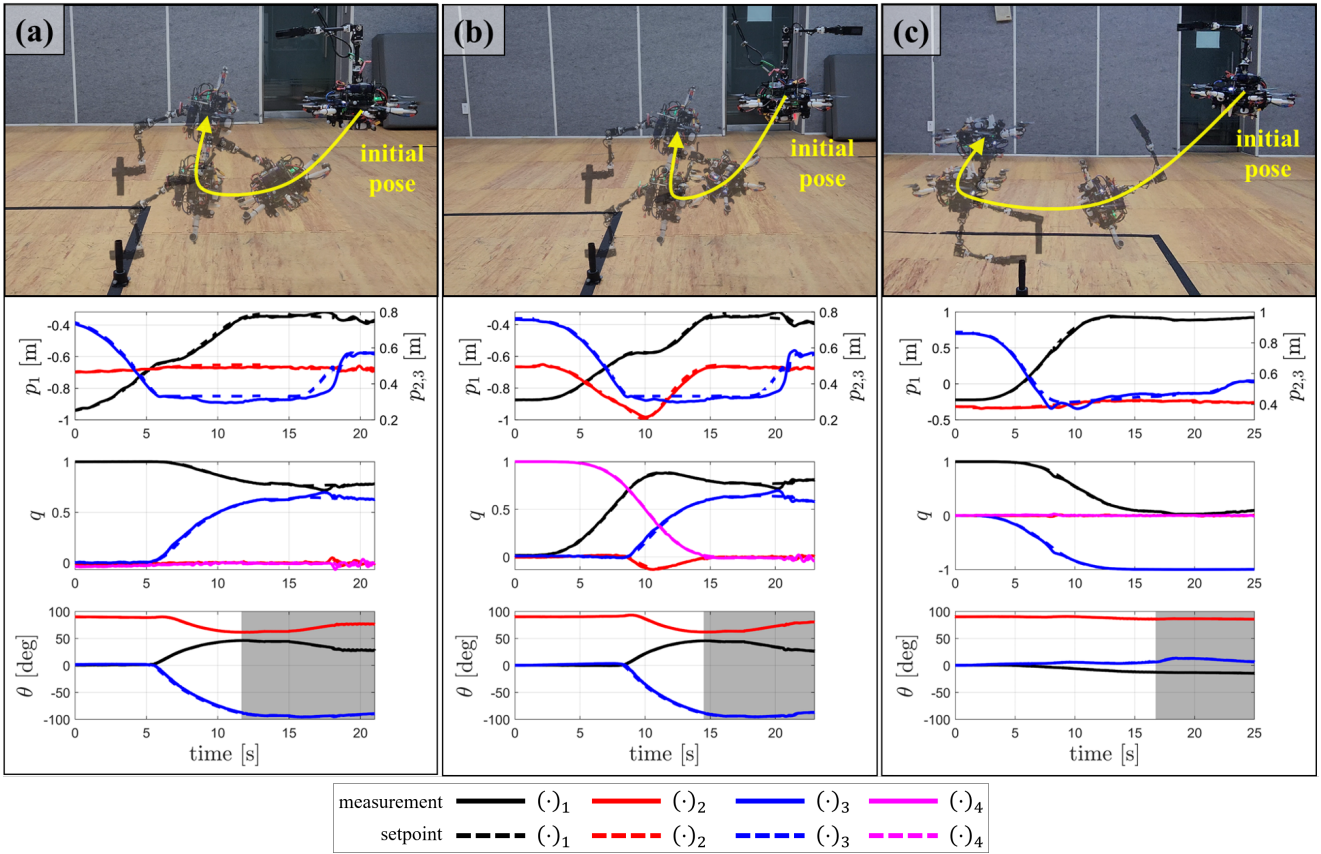


Figure 7. Results of Experiment 2: grasping-and-pulling an object on the ground. The alphabets (a), (b) and (c) indicate to which scenario the figure corresponds to: (a) ground-basic, (b) ground-yaw, and (c) ground-pitch. We use quaternion $q = [q_w, q_x, q_y, q_z]$ to represent the orientation of the multirotor base.

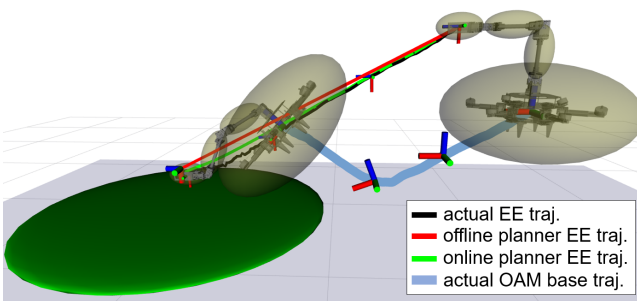


Figure 8. Visualization of trajectories computed by the whole-body motion planner in Experiment 3 setting (a) table-far. The blue line indicates the motion of the multirotor base, and the red and green lines are end-effector trajectories computed by the offline and online planner. The black line is the actual trajectory traversed by the end-effector.

7 Conclusion

In this work, we presented a control and planning framework to enable mobile manipulation with arbitrary base position and orientation. To achieve this objective, we first constructed an omnidirectional aerial manipulator composed of an omnidirectional multirotor and a multi-DoF robotic arm. Then, a geometric robust controller is proposed for the multirotor base which we call a geometric robust integral of the tanh of the error (gRITE) controller. The controller is designed to ensure sufficient performance in the presence of external disturbance including aerodynamic

effect, interaction wrench, and the uncertain motion of the robotic arm. The stability showed that the proposed controller can guarantee arbitrarily small error bound by choosing sufficiently large control gains. Next, a two-step trajectory-optimization-based whole-body motion planning algorithm was proposed while taking omnidirectionality of the OAM and physical constraints including collision avoidance into account. We composed the two offline and online planning phases to formulate a numerically stable optimization problem.

The proposed control and whole-body motion planning framework is validated in hardware experiments. In the first experiment, we compared the proposed controller with a nonlinear PID controller. The proposed controller outperformed the counterpart by showing better regulation performance in the presence of external disturbance by the manipulator. The second and third experiments demonstrated effectiveness of the proposed framework in precise manipulation where the OAM conducted grasping-and-pulling of an object on 1) the ground and 2) a table. We accomplished precise manipulation even in the presence of external disturbance involving ground effect while whole-body motion was exploited in realizing abidance to physical constraints and task completion. During the experiments of precise manipulation, the OAM maintained stable flight around the pitch angle over 90° and even 180° , showing mobile manipulation in arbitrary base pose.

As a future work, we aim to explore collaborative transportation where multiple OAMs transport a common object

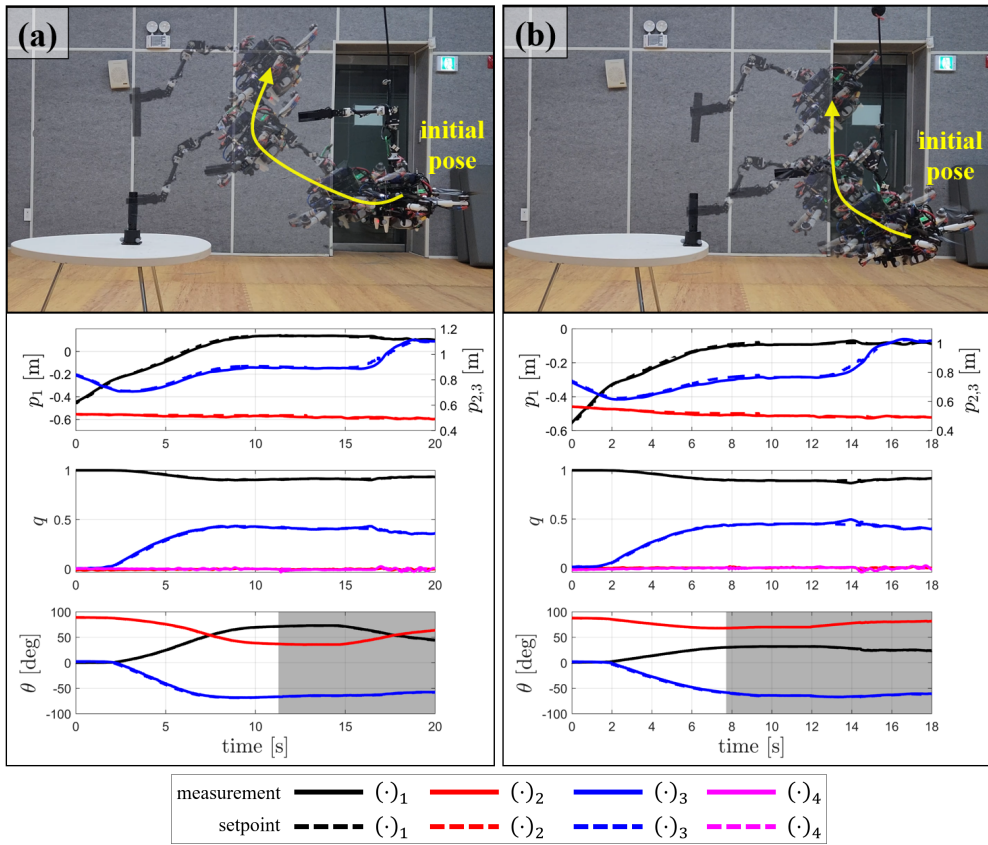


Figure 9. Results of Experiment 3: grasping-and-pulling an object on a table. The alphabets (a) and (b) indicate to which scenario the figure corresponds to: (a) table-far, (b) table-close. We use quaternion $q = [q_w, q_x, q_y, q_z]$ to represent the orientation of the multirotor base.

while each agent exploiting the enlarged workspace. Compared to aerial manipulators based on conventional underactuated multirotors, the additional advantage of the OAMs' enlarged workspace would enhance manipulability of the transporting object, particularly in confined environments.

References

- Allenspach M, Bodie K, Brunner M, Rinsoz L, Taylor Z, Kamel M, Siegwart R and Nieto J (2020) Design and optimal control of a tiltrotor micro-aerial vehicle for efficient omnidirectional flight. *The International Journal of Robotics Research* 39(10–11): 1305–1325.
- Andersson JA, Gillis J, Horn G, Rawlings JB and Diehl M (2019) Casadi: a software framework for nonlinear optimization and optimal control. *Mathematical Programming Computation* 11: 1–36.
- Arcari E, Minniti MV, Scampicchio A, Carron A, Farshidian F, Hutter M and Zeilinger MN (2023) Bayesian multi-task learning mpc for robotic mobile manipulation. *IEEE Robotics and Automation Letters*.
- Bodie K, Brunner M, Pantic M, Walser S, Pfändler P, Angst U, Siegwart R and Nieto J (2021a) Active interaction force control for contact-based inspection with a fully actuated aerial vehicle. *IEEE Transactions on Robotics* 37(3): 709–722.
- Bodie K, Tognon M and Siegwart R (2021b) Dynamic end effector tracking with an omnidirectional parallel aerial manipulator. *IEEE Robotics and Automation Letters* 6(4): 8165–8172.
- Brescianini D and D’Andrea R (2018) Computationally efficient trajectory generation for fully actuated multirotor vehicles. *IEEE Transactions on Robotics* 34(3): 555–571.
- Brunner M, Rizzi G, Studiger M, Siegwart R and Tognon M (2022) A planning-and-control framework for aerial manipulation of articulated objects. *IEEE Robotics and Automation Letters* 7(4): 10689–10696.
- Chiu JR, Sleiman JP, Mittal M, Farshidian F and Hutter M (2022) A collision-free mpc for whole-body dynamic locomotion and manipulation. In: *2022 International Conference on Robotics and Automation (ICRA)*. IEEE, pp. 4686–4693.
- Cuniato E, Geles I, Zhang W, Andersson O, Tognon M and Siegwart R (2023) Learning to open doors with an aerial manipulator. In: *IEEE/RSJ International Conference on Intelligent Robots and Systems (IROS)*. IEEE, pp. 6942–6948.
- Deng W and Yao J (2021) Asymptotic tracking control of mechanical servosystems with mismatched uncertainties. *IEEE/ASME Transactions on Mechatronics* 26(4): 2204–2214.
- Ding Y, Pandala A, Li C, Shin YH and Park HW (2021) Representation-free model predictive control for dynamic motions in quadrupeds. *IEEE Transactions on Robotics* 37(4): 1154–1171.
- Goodarzi F, Lee D and Lee T (2013) Geometric nonlinear pid control of a quadrotor uav on se (3). In: *2013 European control conference (ECC)*. IEEE, pp. 3845–3850.
- Gu X, Xian B and Wang Y (2022) Agile flight for a quadrotor via robust geometry control: Theory and experimental verification. *International Journal of Robust and Nonlinear Control* 32(7): 4236–4250.

- HSL A (2007) collection of fortran codes for large-scale scientific computation. See <http://www.hsl.rl.ac.uk>.
- Hua H, Fang Y, Zhang X and Lu B (2021) A novel robust observer-based nonlinear trajectory tracking control strategy for quadrotors. *IEEE Transactions on Control Systems Technology* 29(5): 1952–1963.
- Huber F, Kondak K, Krieger K, Sommer D, Schwarzbach M, Laiacker M, Kossyk I, Parusel S, Haddadin S and Albu-Schäffer A (2013) First analysis and experiments in aerial manipulation using fully actuated redundant robot arm. In: *2013 IEEE/RSJ Int. Conf. on Intell. Robot. and Syst.* IEEE, pp. 3452–3457.
- Jia F, Wang X and Zhou X (2019) Robust adaptive prescribed performance control for a class of nonlinear pure-feedback systems. *International Journal of Robust and Nonlinear Control* 29(12): 3971–3987.
- Kalabić UV, Gupta R, Di Cairano S, Bloch AM and Kolmanovsky IV (2017) Mpc on manifolds with an application to the control of spacecraft attitude on so (3). *Automatica* 76: 293–300.
- Kamaldin N, Chen SL, Teo CS, Lin W and Tan KK (2019) A novel adaptive jerk control with application to large workspace tracking on a flexure-linked dual-drive gantry. *IEEE Transactions on Industrial Electronics* 66(7): 5353–5363.
- Kamel M, Verling S, Elkhatib O, Sprecher C, Wulkop P, Taylor Z, Siegwart R and Gilitschenski I (2018) The voliro omniorientational hexacopter: An agile and maneuverable tiltable-rotor aerial vehicle. *IEEE Robot. Autom. Mag.* 25(4): 34–44.
- Khalil HK and Grizzle JW (2002) *Nonlinear systems*, volume 3. Prentice hall Upper Saddle River, NJ.
- Kidambi KB, Fermüller C, Aloimonos Y and Xu H (2021) Robust nonlinear control-based trajectory tracking for quadrotors under uncertainty. *IEEE Control Systems Letters* 5(6): 2042–2047.
- Kim C (2023) ROS package for error state kalman filter. URL https://github.com/ChanghyeonKim93/error_state_kalman_filter_ros.
- Kim S, Choi S, Kim H, Shin J, Shim H and Kim HJ (2017) Robust control of an equipment-added multirotor using disturbance observer. *IEEE Transactions on Control Systems Technology* 26(4): 1524–1531.
- Lee D, Byun J and Kim HJ (2022) Rise-based trajectory tracking control of an aerial manipulator under uncertainty. *IEEE Control Systems Letters* 6: 3379–3384.
- Lee D, Seo H, Jang I, Lee SJ and Kim HJ (2021) Aerial manipulator pushing a movable structure using a dob-based robust controller. *IEEE Robotics and Automation Letters* 6(2): 723–730.
- Lee D, Seo H, Kim D and Kim HJ (2020) Aerial manipulation using model predictive control for opening a hinged door. In: *2020 IEEE International Conference on Robotics and Automation (ICRA)*. IEEE, pp. 1237–1242.
- Lee H and Kim HJ (2017) Estimation, control, and planning for autonomous aerial transportation. *IEEE Transactions on Industrial Electronics* 64(4): 3369–3379.
- Lee T, Leok M and McClamroch NH (2010) Geometric tracking control of a quadrotor uav on se (3). In: *49th IEEE conference on decision and control (CDC)*. IEEE, pp. 5420–5425.
- Liang J, Chen Y, Wu Y, Miao Z, Zhang H and Wang Y (2023) Adaptive prescribed performance control of unmanned aerial manipulator with disturbances. *IEEE Transactions on Automation Science and Engineering* 20(3): 1804–1814.
- Lynch KM and Park FC (2017) *Modern robotics*. Cambridge University Press.
- Meduri A, Shah P, Viereck J, Khadiv M, Havoutis I and Righetti L (2023) Biconmp: A nonlinear model predictive control framework for whole body motion planning. *IEEE Transactions on Robotics* 39(2): 905–922.
- Minniti MV, Farshidian F, Grandia R and Hutter M (2019) Whole-body mpc for a dynamically stable mobile manipulator. *IEEE Robotics and Automation Letters* 4(4): 3687–3694.
- Nava G, Sablé Q, Tognon M, Pucci D and Franchi A (2020) Direct force feedback control and online multi-task optimization for aerial manipulators. *IEEE Robotics and Automation Letters* 5(2): 331–338.
- Ollero A, Tognon M, Suarez A, Lee D and Franchi A (2022) Past, present, and future of aerial robotic manipulators. *IEEE Transactions on Robotics* 38(1): 626–645. DOI:10.1109/TRO.2021.3084395.
- Polycarpou MM and Ioannou PA (1996) A robust adaptive nonlinear control design. *Automatica* 32(3): 423–427.
- Ryll M, Muscio G, Pierri F, Cataldi E, Antonelli G, Caccavale F, Bicego D and Franchi A (2019) 6d interaction control with aerial robots: The flying end-effector paradigm. *The International Journal of Robotics Research* 38(9): 1045–1062.
- Seo H, Lee D, Son CY, Tomlin CJ and Kim HJ (2019) Robust trajectory planning for a multirotor against disturbance based on hamilton-jacobi reachability analysis. In: *2019 IEEE/RSJ International Conference on Intelligent Robots and Systems (IROS)*. IEEE, pp. 3150–3157.
- Shin J, Kim HJ, Kim Y and Dixon WE (2011) Autonomous flight of the rotorcraft-based uav using rise feedback and nn feedforward terms. *IEEE Transactions on control systems technology* 20(5): 1392–1399.
- Sleiman JP, Farshidian F, Minniti MV and Hutter M (2021) A unified mpc framework for whole-body dynamic locomotion and manipulation. *IEEE Robotics and Automation Letters* 6(3): 4688–4695.
- Son CY, Seo H, Jang D and Kim HJ (2020) Real-time optimal trajectory generation and control of a multi-rotor with a suspended load for obstacle avoidance. *IEEE Robotics and Automation Letters* 5(2): 1915–1922.
- Su Y, Li J, Jiao Z, Wang M, Chu C, Li H, Zhu Y and Liu H (2023) Sequential manipulation planning for overactuated unmanned aerial manipulators. In: *2023 IEEE/RSJ International Conference on Intelligent Robots and Systems (IROS)*. IEEE, pp. 6905–6911.
- Sun S, Romero A, Foehn P, Kaufmann E and Scaramuzza D (2022) A comparative study of nonlinear mpc and differential-flatness-based control for quadrotor agile flight. *IEEE Transactions on Robotics* 38(6): 3357–3373.
- Tognon M, Cataldi E, Chavez HAT, Antonelli G, Cortés J and Franchi A (2018) Control-aware motion planning for task-constrained aerial manipulation. *IEEE Robotics and Automation Letters* 3(3): 2478–2484.
- Tognon M, Chávez HAT, Gasparin E, Sablé Q, Bicego D, Mallet A, Lany M, Santi G, Revaz B, Cortés J et al. (2019) A truly-redundant aerial manipulator system with application to push-and-slide inspection in industrial plants. *IEEE Robotics and Automation Letters* 4(2): 1846–1851.

- Wang M, Chen Z, Guo K, Yu X, Zhang Y, Guo L and Wang W (2023) Millimeter-level pick and peg-in-hole task achieved by aerial manipulator. *IEEE Transactions on Robotics*.
- Wehbeh J and Sharf I (2022) An mpc formulation on $so(3)$ for a quadrotor with bidirectional thrust and nonlinear thrust constraints. *IEEE Robotics and Automation Letters* 7(2): 4945–4952.
- Welde J, Paulos J and Kumar V (2021) Dynamically feasible task space planning for underactuated aerial manipulators. *IEEE Robotics and Automation Letters* 6(2): 3232–3239.
- Xian B, Dawson DM, de Queiroz MS and Chen J (2004) A continuous asymptotic tracking control strategy for uncertain nonlinear systems. *IEEE Transactions on Automatic Control* 49(7): 1206–1211.
- Xian B and Zhang Y (2016) A new smooth robust control design for uncertain nonlinear systems with non-vanishing disturbances. *International Journal of Control* 89(6): 1285–1302.
- Yu Y, Li P and Gong P (2020) Finite-time geometric control for underactuated aerial manipulators with unknown disturbances. *Int. J. of Robust and Nonlinear Control* 30(13): 5040–5061.
- Zhang Z, Yang S, Chen S, Luo Y, Yang H and Liu Y (2020) A vector-based constrained obstacle avoidance scheme for wheeled mobile redundant robot manipulator. *IEEE Transactions on Cognitive and Developmental Systems* 13(3): 465–474.
- Zhao M, Kawasaki K, Anzai T, Chen X, Noda S, Shi F, Okada K and Inaba M (2018) Transformable multirotor with two-dimensional multilinks: Modeling, control, and whole-body aerial manipulation. *The International Journal of Robotics Research* 37(9): 1085–1112.
- Zhao M, Okada K and Inaba M (2023) Versatile articulated aerial robot dragon: Aerial manipulation and grasping by vectorable thrust control. *The International Journal of Robotics Research* 42(4-5): 214–248.

8 Appendix

8.1 Definition of A in subsection 3.2

We divide the matrix \mathbf{A} into two submatrices $\mathbf{A}_1, \mathbf{A}_2 \in \mathbb{R}^{6 \times 6}$ as $\mathbf{A} = [\mathbf{A}_1 \quad \mathbf{A}_2]$ where $\mathbf{A}_1, \mathbf{A}_2$ are defined as

$$\mathbf{A}_1 = \begin{bmatrix} 0 & -c\frac{\pi}{3} & 0 & -1 & 0 & -c\frac{\pi}{3} \\ 0 & s\frac{\pi}{3} & 0 & 0 & 0 & -s\frac{\pi}{3} \\ 1 & 0 & 1 & 0 & 1 & 0 \\ -Lc\frac{\pi}{3} & k_f c\frac{\pi}{3} & -L & -k_f & -Lc\frac{\pi}{3} & k_f c\frac{\pi}{3} \\ Ls\frac{\pi}{3} & -k_f s\frac{\pi}{3} & 0 & 0 & -Ls\frac{\pi}{3} & k_f s\frac{\pi}{3} \\ -k_f & -L & k_f & -L & -k_f & -L \end{bmatrix}$$

$$\mathbf{A}_2 = \begin{bmatrix} 0 & c\frac{\pi}{3} & 0 & 1 & 0 & c\frac{\pi}{3} \\ 0 & -s\frac{\pi}{3} & 0 & 0 & 0 & s\frac{\pi}{3} \\ 1 & 0 & 1 & 0 & 1 & 0 \\ Lc\frac{\pi}{3} & k_f c\frac{\pi}{3} & L & -k_f & Lc\frac{\pi}{3} & k_f c\frac{\pi}{3} \\ -Ls\frac{\pi}{3} & -k_f s\frac{\pi}{3} & 0 & 0 & Ls\frac{\pi}{3} & k_f s\frac{\pi}{3} \\ k_f & -L & -k_f & -L & k_f & -L \end{bmatrix}.$$

Here, $L, k_f \in \mathbb{R}_{>0}$ are constant values denoting half of the maximal length between any two rotors and the thrust to torque ratio of a single rotor, respectively. In our experiment, we set $L = 0.018$ m and $k_f = 0.015$ m.

8.2 Proof of Lemma 3

Proof. Using the Comparison Lemma (Khalil and Grizzle 2002, Lemma 3.4), $s(t) \leq \bar{s}(t)$ where $\bar{s}(t)$ satisfies $\dot{\bar{s}} = -\alpha(\bar{s}) + \alpha(c_s)$ and $\bar{s}(0) = s(0)$. Considering a positive definite function $H = \frac{1}{2}(\bar{s} - c_s)^2$ for $\bar{s} - c_s$, its time-derivative is computed as $\dot{H} = -(\bar{s} - c_s)(\alpha(\bar{s}) - \alpha(c_s))$, which is negative definite. Thus, using (Khalil and Grizzle 2002, Theorem 4.9), there exists $\beta(\cdot, \cdot) \in \mathcal{KL}$ such that $\bar{s}(t) \leq \beta(\bar{s}(0) - c_s, t) + c_s \forall t \geq 0$. Since $s(t) \geq \bar{s}(t) \forall t$ and $\bar{s}(0) = s(0)$, this finishes the proof.

8.3 Proof of Theorem 1

Proof. By using (10), Lemma 2 and Young's inequality for obtaining $\mathbf{e}_p^\top \mathbf{e}_{t1} \leq \frac{1}{2}\|\mathbf{e}_p\|^2 + \frac{1}{2}\|\mathbf{e}_{t1}\|^2$ and $\mathbf{e}_{t2}^\top \tilde{N}_t \leq \lambda_m(\mathbf{K}_{ti})\|\mathbf{e}_{t2}\|^2 + \frac{1}{4\lambda_m(\mathbf{K}_{ti})}\|\tilde{N}_t\|^2$, \dot{V}_t can be further arranged as

$$\dot{V}_t \leq -\left(\eta_t^* - \frac{\mu_t^2}{4\lambda_m(\mathbf{K}_{ti})}\right)\|\mathbf{e}_t\|^2 + \sum_{i=1}^n \frac{\Gamma_{t,i}}{\Theta_{t,i}} c_i. \quad (23)$$

Meanwhile, by Lemma 1, V_t satisfies the lower and upper bounds of

$$\eta_t\|\mathbf{e}_t\|^2 \leq V_t(t) \leq \bar{\eta}_t(\|\mathbf{e}_t\|) + \sigma_t \quad (24)$$

where

$$\sigma_t = \sum \frac{\Gamma_{t,i}}{\Theta_{t,i}} \ln 2, \quad \eta_t = \min\left\{\frac{1}{2}m, \frac{1}{2}\right\}$$

$$\bar{\eta}_t(\|\mathbf{e}_t\|) = \max\left\{\frac{1}{2}m, \frac{1}{2}\right\}\|\mathbf{e}_t\|^2 + \sum_{i=1}^n (\Gamma_{t,i} + \|N_{td,i}\|_\infty)|e_{t1,i}|.$$

Using (24) and the fact that $(\alpha(a+b))^2 \leq (\alpha(2a))^2 + (\alpha(2b))^2$ for any $\alpha(\cdot) \in \mathcal{K}_\infty$ and $a, b \in \mathbb{R}$, and $\bar{\eta}_t^{-1}(\cdot) \in \mathcal{K}_\infty$, i.e. the inverse of $\bar{\eta}_t(\cdot) \in \mathcal{K}_\infty$,

$$\|\mathbf{e}_t\|^2 \geq \begin{cases} \{\bar{\eta}_t^{-1}(V_t - \sigma_t)\}^2 & \text{if } V_t \geq \sigma_t \\ 0 & \text{if } V_t < \sigma_t \end{cases}$$

$$\geq \begin{cases} \{\bar{\eta}_t^{-1}(V_t/2)\}^2 - \{\bar{\eta}_t^{-1}(\sigma_t)\}^2 & \text{if } V_t \geq \sigma_t \\ 0 & \text{if } V_t < \sigma_t \end{cases}.$$

Then, by applying the control gain condition and the above inequality,

$$\dot{V}_t \leq -\Omega_t(V_t) + \Omega_t(\Xi_t)$$

where

$$\Omega_t(V_t) = \frac{\eta_t^*}{2}(\bar{\eta}_t^{-1}(V_t/2))^2 \in \mathcal{K}_\infty$$

$$C_t(\sigma_t) = \frac{\eta_t^*}{2}(\bar{\eta}_t^{-1}(\sigma_t))^2 + \frac{c}{\ln 2}\sigma_t$$

and $\Xi_t = \Omega_t^{-1}(C_t(\sigma_t))$. By applying Lemma 3, the following upper bound for V_t can be obtained, and that for $\|\mathbf{e}_t\|$ also naturally follows from (24):

$$V_t \leq \beta_t(|V_t(0) - \Xi_t|, t) + \Xi_t,$$

$$\|\mathbf{e}_t\| \leq \sqrt{\frac{1}{\eta_t} \beta_t(|V_t(0) - \Xi_t|, t) + \frac{\Xi_t}{\eta_t}}$$

where $\beta_t(\cdot, \cdot) \in \mathcal{KL}$. Since the ultimate bound $\sqrt{\frac{\Xi_t}{\eta_t}}$ can be made arbitrarily small by taking sufficiently large Θ_t , the proof is complete.

8.4 Proof of Lemma 4

Proof. Finite $\Gamma_{r,i}$ exists by the Assumption 1. Since $\Psi(t) \leq \psi < 2$ for $t \in [t_1, t_2]$, $\frac{1}{2}\|\mathbf{e}_R\|^2 \leq \Psi(t) \leq \frac{1}{2-\psi}\|\mathbf{e}_R\|^2$ holds for all $t \in [t_1, t_2]$ Lee et al. (2010). Then, similar to the result for V_t in (24), the lower and upper bounds of V_r can be computed as

$$\eta_r \|\mathbf{e}_r\|^2 \leq V_r(t) \leq \bar{\eta}_r(\|\mathbf{e}_r\|) + \sigma_r \quad (25)$$

where $\eta_r, \sigma_r > 0$ and $\bar{\eta}_r(\cdot) \in \mathcal{K}_\infty$. Here, we use the fact that Q_r has lower and upper bounds similar to the result of Lemma 1 for Q_t . Similar to (23), \dot{V}_r is upper-bounded by

$$\dot{V}_r \leq - \left(\eta_r^* - \frac{\mu_r^2(\|\mathbf{e}_r\|)}{4\lambda_m(\mathbf{K}_{ri})} \right) \|\mathbf{e}_r\|^2 + \sum \frac{\Gamma_{r,i}}{\Theta_{r,i}} c$$

where we use $\dot{\Psi} = \mathbf{e}_\omega^\top \mathbf{e}_R$. Then, by following the same procedure in Theorem 1, we can show that $\dot{V}_r \leq -\Omega_r(V_r) + \Omega_r(\Xi_r)$ where $\Xi_r = \Omega_r^{-1}(C_r(\sigma_r))$ and

$$\begin{aligned} \Omega_r(V_r) &= \frac{\eta_r^*}{2} (\bar{\eta}_r^{-1}(V_r/2))^2 \in \mathcal{K}_\infty \\ C_r(\sigma_r) &= \frac{\eta_r^*}{2} (\bar{\eta}_r^{-1}(\sigma_r))^2 + \frac{c}{\ln 2} \sigma_r. \end{aligned} \quad (26)$$

The definition of $\beta_r(\cdot, \cdot) \in \mathcal{KL}$ is derived when applying Lemma 3 to (14).

8.5 Proof of Theorem 2

Proof. Let the maximal time interval for $V_r(t) \leq \psi$ is given by $t \in [0, \delta_t]$. Thanks to the initial condition (15) and smoothness of $V_r(t)$, there always exists $\delta_t > 0$. Now, assume that δ_t is finite. Then, since $[0, \delta_t]$ is the maximum time interval, $V_r(\delta_t) = \psi$ and $\dot{V}_r(\delta_t) \geq 0$. However, from Lemma 4, during the time interval $[0, \delta_t]$, the following holds:

$$\dot{V}_r(t) \leq -\Omega_r(V_r(t)) + \Omega_r(\Xi_r).$$

Then,

$$\begin{aligned} \dot{V}_r(\delta_t) &\leq -\Omega_r(V_r(\delta_t)) + \Omega_r(\Xi_r) \\ &= -\Omega_r(\psi) + \Omega_r(\Xi_r) < 0 \end{aligned}$$

where we use $\Xi_r < \psi$. However, this contradicts to $\dot{V}_r(\delta_t) > 0$; thus, $V_r(t) \leq \psi$ holds for all $t \in [0, \infty)$.

From this property of $V_r(t) \leq \psi \forall t \in [0, \infty)$ and the fact that $\Psi \leq V_r$, we can apply Lemma 4 again for the infinite time interval $[0, \infty)$. Then, using Lemma 3 and (25),

$$V_r \leq \beta_r(|V_r(t_0) - \Xi_r|, t - t_0) + \Xi_r \quad (27a)$$

$$\|\mathbf{e}_r\| \leq \sqrt{\frac{1}{\eta_r} \beta_r(|V_r(t_0) - \Xi_r|, t - t_0) + \frac{\Xi_r}{\eta_r}} \quad (27b)$$

where the definitions of $\beta_r(\cdot, \cdot)$ and Ξ_r are in Lemma 4.

The proof is finished by using (27b) which holds $\forall t \in [0, \infty)$ and the fact that the ultimate bound $\sqrt{\frac{\Xi_r}{\eta_r}}$ can be made arbitrarily small by taking sufficiently large Θ_r recalling that $\Xi_r = \Omega_r^{-1}(C_r(\sigma_r))$ and $\sigma_r = \sum \frac{\Gamma_{r,i}}{\Theta_{r,i}} \ln 2$, where the definitions of Ω_r, C_r can be found in (26).

8.6 Definition of ${}^E f_p$ and ${}^E f_R$

The kinematics of translational and rotational motion represented in the continuous time domain are as follows:

$$\begin{aligned} \frac{d}{dt} {}^E \mathbf{p}_d &= {}^E \mathbf{v}_d, & \frac{d}{dt} {}^E \mathbf{v}_d &= {}^E \dot{\mathbf{v}}_d, & \frac{d}{dt} {}^E \dot{\mathbf{v}}_d &= {}^E \ddot{\mathbf{v}}_d \\ \frac{d}{dt} {}^E \mathbf{R}_d &= {}^E \mathbf{R}_d {}^E \boldsymbol{\omega}_d^\wedge, & \frac{d}{dt} {}^E \boldsymbol{\omega}_d &= {}^E \dot{\boldsymbol{\omega}}_d, & \frac{d}{dt} {}^E \dot{\boldsymbol{\omega}}_d &= {}^E \ddot{\boldsymbol{\omega}}_d \end{aligned}$$

We numerically integrate these differential equations using the Runge-Kutta 4th-order method in the offline planning phase to reduce numerical errors. More specifically, for given ${}^E \mathbf{x}_p = [{}^E \mathbf{p}_d; {}^E \mathbf{v}_d; {}^E \dot{\mathbf{v}}_d]$, ${}^E \mathbf{x}_R = ({}^E \mathbf{R}_d, {}^E \boldsymbol{\omega}_d, {}^E \dot{\boldsymbol{\omega}}_d)$, ${}^E \ddot{\mathbf{v}}_d$ and ${}^E \ddot{\boldsymbol{\omega}}_d$, the kinematic models ${}^E f_p$ and ${}^E f_R$ in the discrete time domain can be found below:

$$\begin{aligned} \bar{\mathbf{v}}_1 &= \mathbf{v}_d + 0.5\Delta t \dot{\mathbf{v}}_d, & \dot{\bar{\mathbf{v}}}_1 &= \dot{\mathbf{v}}_d + 0.5\Delta t \ddot{\mathbf{v}}_d \\ \bar{\mathbf{v}}_2 &= \mathbf{v}_d + 0.5\Delta t \dot{\bar{\mathbf{v}}}_1, & \dot{\bar{\mathbf{v}}}_2 &= \dot{\bar{\mathbf{v}}}_1 + 0.5\Delta t \ddot{\mathbf{v}}_d \\ \bar{\mathbf{v}}_3 &= \mathbf{v}_d + \Delta t \dot{\bar{\mathbf{v}}}_2, & \dot{\bar{\mathbf{v}}}_3 &= \dot{\bar{\mathbf{v}}}_2 + \Delta t \ddot{\mathbf{v}}_d \end{aligned}$$

$${}^E f_p = \begin{bmatrix} {}^E \mathbf{p}_d + \Delta t/6(\mathbf{v}_d + 2\bar{\mathbf{v}}_1 + 2\bar{\mathbf{v}}_2 + \bar{\mathbf{v}}_3) \\ {}^E \mathbf{v}_d + \Delta t/6(\dot{\mathbf{v}}_d + 2\dot{\bar{\mathbf{v}}}_1 + 2\dot{\bar{\mathbf{v}}}_2 + \dot{\bar{\mathbf{v}}}_3) \\ {}^E \dot{\mathbf{v}}_d + \Delta t \ddot{\mathbf{v}}_d \end{bmatrix} \quad (28)$$

$$\begin{aligned} \bar{\boldsymbol{\omega}}_1 &= \boldsymbol{\omega}_d + 0.5\Delta t \dot{\boldsymbol{\omega}}_d, & \dot{\bar{\boldsymbol{\omega}}}_1 &= \dot{\boldsymbol{\omega}}_d + 0.5\Delta t \ddot{\boldsymbol{\omega}}_d \\ \bar{\boldsymbol{\omega}}_2 &= \boldsymbol{\omega}_d + 0.5\Delta t \dot{\bar{\boldsymbol{\omega}}}_1, & \dot{\bar{\boldsymbol{\omega}}}_2 &= \dot{\bar{\boldsymbol{\omega}}}_1 + 0.5\Delta t \ddot{\boldsymbol{\omega}}_d \\ \bar{\boldsymbol{\omega}}_3 &= \boldsymbol{\omega}_d + \Delta t \dot{\bar{\boldsymbol{\omega}}}_2, & \dot{\bar{\boldsymbol{\omega}}}_3 &= \dot{\bar{\boldsymbol{\omega}}}_2 + \Delta t \ddot{\boldsymbol{\omega}}_d \end{aligned}$$

$${}^E f_R = \begin{bmatrix} {}^E \mathbf{R}_d \exp(\Delta t/6(\boldsymbol{\omega}_d + 2\bar{\boldsymbol{\omega}}_1 + 2\bar{\boldsymbol{\omega}}_2 + \bar{\boldsymbol{\omega}}_3)^\wedge) \\ {}^E \boldsymbol{\omega}_d + \Delta t/6(\dot{\boldsymbol{\omega}}_d + 2\dot{\bar{\boldsymbol{\omega}}}_1 + 2\dot{\bar{\boldsymbol{\omega}}}_2 + \dot{\bar{\boldsymbol{\omega}}}_3)^\wedge \\ {}^E \dot{\boldsymbol{\omega}}_d + \Delta t \ddot{\boldsymbol{\omega}}_d \end{bmatrix} \quad (29)$$

where $\exp(\cdot)$ is a matrix exponential. We omitted the time index k and the arguments of ${}^E f_p$ and ${}^E f_R$ for simplicity.

8.7 Definition of f_x

The kinematics of OAM in the continuous time domain are represented as the following:

$$\frac{d}{dt} {}^E \mathbf{p}_d = \mathbf{v}_d, \quad \frac{d}{dt} {}^E \mathbf{R}_d = \boldsymbol{\omega}_d, \quad \frac{d}{dt} {}^E \boldsymbol{\theta}_d = \dot{\boldsymbol{\theta}}_d$$

For fast computation, we numerically integrate the above differential equations using the Euler 1st-order method. In other words, for given $\mathbf{x}_d(k) = (\mathbf{p}_d(k), \mathbf{R}_d(k), \boldsymbol{\theta}_d(k))$ and $\mathbf{u}_k = (\mathbf{v}_d(k), \boldsymbol{\omega}_d(k), \dot{\boldsymbol{\theta}}_d(k))$, we consider the following as the definition of $f_x(\mathbf{x}_d(k), \mathbf{u}_d(k))$:

$$\mathbf{f}_x = \begin{bmatrix} \mathbf{p}_d(k) + \Delta t \mathbf{v}_d(k) \\ \mathbf{R}_d(k) \exp(\Delta t(\boldsymbol{\omega}_d(k))^\wedge) \\ \boldsymbol{\theta}_d(k) + \Delta t \dot{\boldsymbol{\theta}}_d(k) \end{bmatrix}. \quad (30)$$